Tying textures of breadcrust bombs to their transport regime and cooling history

Mary C. Benage [a,*], Josef Dufek [a], Wim Degruyter [a], Dennis Geist [b], Karen Harpp [c], Erika Rader [b]

[a] School of Earth and Atmospheric Sciences, Georgia Institute of Technology, Atlanta, GA, USA
[b] Department of Geological Sciences, University of Idaho, Moscow, ID, USA
[c] Department of Geology, Colgate University, Hamilton, NY, USA

ARTICLE INFO

ABSTRACT

The thermal evolution of explosive eruptive events such as volcanic plumes and pyroclastic density currents (PDCs) is reflected in the textures of the material they deposit. Here we evaluate how the rinds of breadcrust bombs can be used as a unique thermometer to examine mafic to intermediate explosive eruptions. These eruptions can produce breadcrust bombs in either PDCs or as projectiles following nearly ballistic trajectories. We develop an integrated model to examine bubble growth, pyroclast cooling, and dynamics of PDCs and projectiles from buoyant plumes. We examine rind development as a function of transport regime (PDC and projectile), transport properties (initial current temperature and current density), and pyroclast properties (initial water content and radius). The model reveals that: 1) rinds of projectile pyroclasts are in general thicker and less vesicular than those of PDC pyroclasts; 2) as the initial current temperature decreases due to initial air entrainment, the rinds on PDC pyroclasts progressively increase in thickness; and 3) rind thickness increases with decreasing water concentration and decreasing clast radius. Therefore, the modeled pyroclast's morphology is dependent not only on initial water concentration but also on the cooling rate, which is determined by the transport regime.

© 2014 Elsevier B.V. All rights reserved.

1. Introduction

Pyroclastic density currents (PDCs) are some of the most destructive volcanic phenomena and understanding the many physical processes associated with these flows has proven difficult. Inherent opacity limitations and hazardous conditions have resulted in relatively poor constraints on flow dynamics, in particular on the thermal evolution. One mechanism that changes the thermal state of the current is entrainment of colder, ambient air (Sparks, 1986; Bursik and Woods, 1996). The extent to which a current will entrain ambient air depends on the particle concentration and concentration gradient, particle size distribution, current shear, and current temperature (Dufek and Bergantz, 2007a). These temporally and spatially variable conditions control the thermal evolution of a PDC, directly influence the total run out distance, and determine deposit characteristics (Hallworth et al., 1993; Bursik and Woods, 1996; Branney and Kokelaar, 2002; Clarke et al., 2002; Wilson and Houghton, 2002; Neri et al., 2003; Scott et al., 2008). To improve our knowledge of the thermal evolution of PDCs, a better understanding and application of thermal proxies in these flows must be developed.

Hot pyroclasts that are deposited from explosive volcanic eruptions, either from ballistic trajectories or PDCs, have the potential to be used as thermal proxies. Each pyroclast has a unique transport path that samples a portion of the volcanic environment (Kaminski and Jaupart, 1997; Vanderkluysen et al., 2012). A breadcrust bomb (see Fig. 1a) may be an especially useful thermal proxy due to its unique texture (Wright et al., 2007; Giachetti et al., 2010). A breadcrust bomb is a pyroclast that has many surface cracks, a dense rind, and a vesicular interior. The surface cracks likely develop as a product of the continual growth of gas bubbles in the hot interior, which causes expansion of the clast and subsequent cracking of the brittle rind (Walker, 1969; Wright et al., 2007). Some surface cracks may also be from thermal contraction or from the stress of impact (Wright et al., 2007). Breadcrust bombs are found in deposits from basaltic to rhyolitic explosive eruptions, typically of Vulcanian style (Walker, 1982; Morrissey and Mastin, 2002; Wright et al., 2007). Some volcanoes that have generated breadcrust bombs are Montserrat (Giachetti et al., 2010), Mayon (Moore and Melson, 1969), Cerro Galan (Wright et al., 2011), Lascar (Calder et al., 2000), Panum Dome (Anderson et al., 1994), Cotopaxi (Pistolesi et al., 2011), Guagua Pichincha (Wright et al., 2007), Tungurahua (Hall et al., 1999; Le Pennec et al., 2008; Douillet et al., 2013), Vulcano (Walker, 1969), and Ngauruhoe (Morrissey and Mastin, 2002). Breadcrust bombs are found as ballistically emplaced clasts in the crater or on the flank of volcanoes (Wright et al., 2007; Giachetti et al., 2010), but some are

---

* Corresponding author at: School of Earth and Atmospheric Sciences, Georgia Institute of Technology, 311 Ferst Drive, Atlanta, GA 30332, USA. Tel.: +1 505 310 4348.
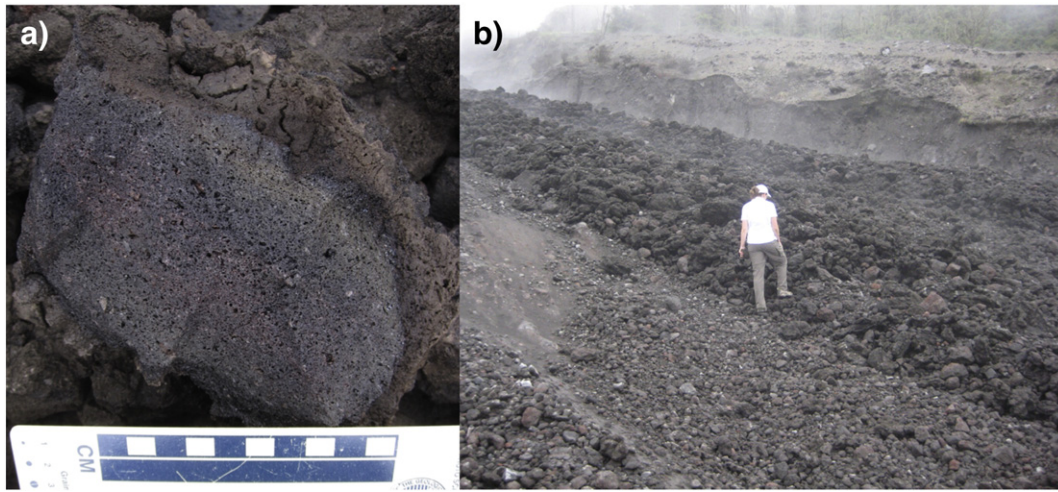E-mail address: mary.benage@eas.gatech.edu (M.C. Benage).

Fig. 1. Breadcrust bombs. a.) An example of a breadcrust bomb with a dense rind from Tungurahua volcano, Ecuador. b.) PDC deposit of breadcrust bombs at Tungurahua volcano, Ecuador.

also found in PDC deposits (Fig. 1b) kilometers away from the vent (Hall et al., 1999; Hall and Mothes, 2008; Giachetti et al., 2010; Samaniego et al., 2011; Douillet et al., 2013). The vesicularity gradient of a breadcrust bomb is hypothesized to be the result of syn-eruptive bubble nucleation and growth, and the quick cooling of the bomb's edge during transport (Walker, 1969, 1982; Giachetti et al., 2010).

The radial distribution of bubble sizes in the clasts can provide insight into each bomb's thermal history. Bubbles grow through diffusion of volatiles into the bubble, where growth and expansion is limited by magmatic viscosity, which changes by orders of magnitude during cooling and solidification (Sparks, 1978; Prousevitch et al., 1993; Proussevitch and Sahagian, 1996; Blower et al., 2001). Bubble nucleation in breadcrust bombs is thought to happen after fragmentation because of the small, isolated bubbles or the lack of bubbles in the rind (Giachetti et al., 2010). Immediately after eruption and fragmentation, breadcrust bombs are often above the glass transition temperature, the kinetic limit at which the material transitions from a viscous liquid to a glass (Gottsmann et al., 2002; Giordano et al., 2005). As the clast cools, viscosity increases and parts of the clast will cross the glass transition temperature. The increase in viscosity slows bubble growth, and bubble growth is terminated at high viscosities or when the temperature crosses the glass transition temperature. Therefore, the preserved radial bubble size distribution in the bomb provides a textural indicator of the relative timing between fragmentation and quenching (Giachetti et al., 2010). The radially dependent bubble size distribution within a given breadcrust bomb is proposed to be a function of bubble nucleation delay, bubble growth rate, cooling rate, and viscosity (Walker, 1969, 1982; Hoblitt and Harmon, 1993; Giachetti et al., 2010). Examining textural features of breadcrust bomb rinds after an eruption, when the depositional location of the pyroclast is known, provides an opportunity to retrace the thermal history of the pyroclast and of the eruption itself.

A combination of physical and mathematical models have been used to look at the cooling of pyroclasts that fell vertically (Thomas and Sparks, 1992), had ballistic trajectories (Capaccioni and Cuccoli, 2005; Wright et al., 2007), or were entrained within an eruption column (Kaminski and Jaupart, 1997; Hort and Gardner, 2000). Previous cooling models of falling pyroclasts have used convective and radiative heat transfer boundary conditions and conductive cooling in the clast interior (Thomas and Sparks, 1992). More recent models expanded on this by adding a ballistic transport model with flight path and velocity to calculate the cooling of pyroclasts on a parabolic trajectory (Capaccioni and Cuccoli, 2005; Wright et al., 2007). Wright et al. (2007) compared known rind thicknesses of breadcrust bombs

from field data to their cooling model to determine the time required for the rind to cool below the glass transition temperature. The time for the rind to cool below the glass transition temperature was used as an approximation for rind formation time. The comparison suggests that rinds form relatively quickly (less than 45 s) after eruption and that some rinds on finely breadcrusted bombs form before impact.

A limited number of studies examine the interaction between cooling rates and syn-eruptive bubble growth. The model by Hort and Gardner (2000) on pumice cooling and bubble growth showed that water loss in pumice depends on the cooling rate. Pumice was almost completely degassed if the ratio of the cooling timescale to the degassing timescale was greater than approximately 50 (Hort and Gardner, 2000). A pumice clast was less vesicular at the edge compared to its interior because of rapid cooling and viscous quenching on clast margins (Kaminski and Jaupart, 1997). The impact of these timescales on textures stresses the need to couple numerical models of cooling and bubble growth to better interpret pyroclast textures. The pyroclast's transport path through the local environment will influence its final texture. All of these previous cooling models focus on either a parabolic path with no collisions or a collision-free fall through a uniform temperature environment. The examination of pyroclast cooling while entrained in a PDC has not been studied. No existing numerical model compares how different travel paths, such as ballistic versus PDC transport, affect a pyroclast's cooling history and, therefore, its texture.

In this study, a model of the thermal history and rind thickness of breadcrust bombs is developed to determine if path- and temperature-dependent textural information is imparted on multiple pyroclasts when transported either as projectiles in a buoyant eruption plume or within the body of a PDC. Throughout the text, pyroclasts entrained in PDCs will be referred to as PDC pyroclasts or PDC. The pyroclasts that are ballistically ejected out of a buoyant plume will be referred to as projectile pyroclasts or projectile. To evaluate how the cooling history influences rind thickness, we build on the pyroclast cooling models presented in Thomas and Sparks (1992), Capaccioni and Cuccoli (2005), and Wright et al. (2007) by adding a detailed transport system and a coupled model of cooling, viscosity, and bubble growth for individual pyroclasts. In each pyroclast, the radial change in bubble size allows for an explicit definition of rind thickness, where the rind contains the smallest bubbles. We also examine how varying the initial water concentration in the pyroclast affects the rind thickness. In this work, we focus on the end-member conditions of projectile pyroclasts ejected primarily through a cool, ambient atmosphere and pyroclasts transported in hot PDCs with variable entrainment histories. Here we do not focus on a specific eruption, but rather evaluate

general trends in textural development associated with variable transport histories.

2. Methods

A coupled, multi-scale model is constructed to assess the effect transport path has on a breadcrust bomb's rind thickness and radial bubble size distribution. Development of the breadcrust bomb is modeled by combining three models of different scales that affect its evolution: 1.) macro-scale: pyroclast transport in a multiphase current; 2.) pyroclast-scale: surface heat loss and interior conductive cooling; and 3.) micro-scale: bubble growth. A model schematic is shown in Fig. 2.

2.1. Macro-scale model

We apply a multiphase Eulerian–Eulerian–Lagrangian (EEL) model, modified from MFIX (Multiphase Flow with Interphase eXchanges (Syamlal et al., 1993)), for volcanic currents (Dufek and Berganz, 2007a) to simulate evolving particle concentration, thermal environment, physical dynamics, and the relative motion of clasts in two end-member currents: projectile pyroclasts from buoyant plumes and pyroclasts entrained in PDCs. The EEL model has previously been used to model PDCs and their deposits (Dufek and Berganz, 2007a, 2007b; Dufek et al., 2009) and has been validated by comparison to direct numerical simulations (DNS) of gravity currents and experiments (Dufek and Berganz, 2007a). This multiphase model solves the continuum equations for mass, momentum, and energy, as well as related constitutive equations. For the PDC simulations, the resolution is 20 m by 5 m and the simulation area is 8070 m by 2000 m, both respectively along the horizontal and vertical axis. For the buoyant eruption with projectiles, the resolution is 20 m by 20 m and the simulation area is 8070 m by 6000 m, respectively along the horizontal and vertical axis. For the two transport regimes, the same topography of a gentle, smooth slope is used (See Figs. 3 and 4 for an example of the topographic profile).

The model uses two continuum (Eulerian) phases: a particle phase that represents the fine particles (particle diameter is 5.0×10^{-5} m for PDC simulations and 1.0×10^{-4} m for the buoyant plume simulations) and a gas phase. The particle diameters for PDC and buoyant plume ash are selected to have a Stokes number less than ~0.1 so that the fine particle phase will act as tracers of the fluid flow. The ash phase here approximates particles generated both from the initial fragmentation event as well as those generated by post-fragmentation conduit processes (Dufek et al., 2012) and during transport (Dufek and Manga, 2008). The particle and gas phases are two-way coupled by drag forces. The particle phase can interact with the gas phase, internally within its phase as a result of collisions or frictional interaction, and with the substrate. The collisional transfer of momentum is assumed to be binary and inelastic, and frictional stresses are assumed when the local volume fraction of particles exceeds close packing (here assumed to be 0.5 volume fraction) (Dufek and Berganz, 2007a). The conservation equations are solved by finite volume methods.

The governing equations are the conservation of mass for both phases,

$$\frac{\partial}{\partial t}\left(\alpha_g \rho_g\right) + \frac{\partial}{\partial x_i}\left(\alpha_g \rho_g u_{g,i}\right) = 0, \tag{1}$$

$$\frac{\partial}{\partial t}\left(\alpha_s \rho_s\right) + \frac{\partial}{\partial x_i}\left(\alpha_s \rho_s u_{s,i}\right) = 0, \tag{2}$$

the conservation of energy for both phases,

$$\alpha_g \rho_g c_{P,g}\left(\frac{\partial T_g}{\partial t} + u_{g,i}\frac{\partial T_g}{\partial x_i}\right) = \frac{\partial q_g}{\partial x_i} - \overline{H}_{gs}, \tag{3}$$

$$\alpha_s \rho_s c_{P,s}\left(\frac{\partial T_s}{\partial t} + u_{s,i}\frac{\partial T_s}{\partial x_i}\right) = \frac{\partial q_s}{\partial x_i} + \overline{H}_{gs}, \tag{4}$$
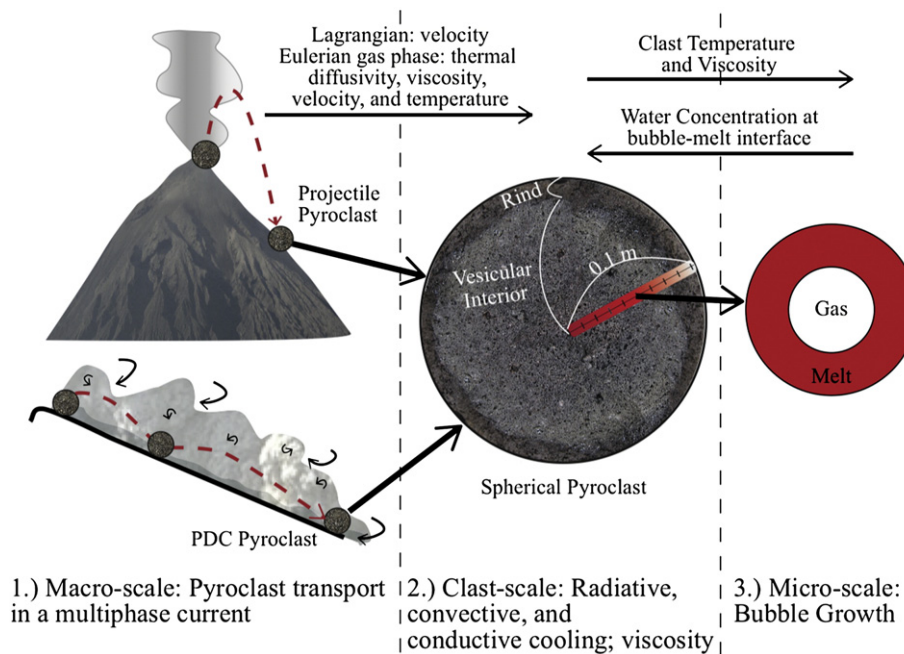

Fig. 2. Model schematic (not to scale). 1.) Macro-scale: transport of pyroclasts as either projectile pyroclasts that erupt from a buoyant plume or as pyroclasts entrained in a PDC. 2.) Pyroclast-scale: the cooling of the isotropic, spherical clast from convective and radiative heat transfer to the surrounding environment and conductive cooling in the interior. The clast composition, water content (changing due to bubble growth) and temperature (changing due to cooling) are used to calculate viscosity and glass transition temperature. 3.) Micro-scale: The bubble growth model in which growth is limited by viscosity and diffusion, and is halted once the temperature is lower then the calculated glass transition temperature.

and the conservation of momentum for both phases,

$$\frac{\partial}{\partial t}\left(\alpha_g \rho_g u_{g,i}\right) + \frac{\partial}{\partial x_i}\left(\alpha_g \rho_g u_{g,i} u_{g,j}\right) = \frac{\partial P_g}{\partial x_i}\delta_{ij} + \frac{\partial \tau_{g,ij}}{\partial x_j} + I_i + \alpha_g \rho_g g_i \delta_{i2}, \quad (5)$$

$$\frac{\partial}{\partial t}\left(\alpha_s \rho_s u_{s,i}\right) + \frac{\partial}{\partial x_i}\left(\alpha_s \rho_s u_{s,i} u_{s,j}\right) = \frac{\partial P_s}{\partial x_i}\delta_{ij} + \frac{\partial \tau_{s,ij}}{\partial x_j} - I_i + \alpha_s \rho_s g_i \delta_{i2}. \quad (6)$$

See Table 1 for definition of symbols.

In addition to the two Eulerian phases, a Lagrangian phase is modeled to simulate the path and environment of a pyroclast during an eruption. Each individual Lagrangian particle is influenced by its local environment, which changes temporally and spatially. To track the particles, the equation of motion of each particle,

$$m_s \frac{du_{s,i}}{dt} = F_{g,i} + F_{s,i} + g\left(m_s - m_f\right)\delta_{i2}, \quad (7)$$

is solved and is coupled to the Eulerian phases through the drag terms, where F_g is the drag force from the gas phase, F_s is the force from the collision of small particles, m_s is the mass of the particle, m_f is the mass of the gas displaced by the particle, and the i terms are index notation (Maxey and Riley, 1983; Burgisser et al., 2005; Dufek et al., 2009). See Table 1 for further explanation of symbols. We examine 1000 Lagrangian particles (i.e., pyroclasts) per simulation. The Lagrangian particles are the same size to facilitate comparison between simulations (acknowledging that real eruptions have complex distributions of large clasts). The EEL model calculates and records the environmental information the Lagrangian particle experiences by interpolating the velocity, gas viscosity, gas heat capacity, gas density, and mean-temperature fields simulated through the Eulerian component to the specific particle location. To model breadcrust bomb morphology, these environmental conditions are used to calculate the cooling of the clast.

2.2. Clast-scale

2.2.1. Clast cooling

The cooling of individual pyroclasts is modeled by solving for heat loss due to convective and radiative heat transfer at the surface and conductive cooling within the clast. Convective and radiative cooling is assumed to only take place at the surface and is not calculated radially within the clast. This assumption has been determined to be appropriate for cooling of pumiceous pyroclasts, where it was determined that interior convective and radiative heat transfer is negligible (Thomas and Sparks, 1992; Tait et al., 1998; Hort and Gardner, 2000). Clasts are assumed to be spherical, isotropic, uniform in composition, and constant in size (i.e. we assume no radial expansion due to bubble growth). We further assume the bulk material properties of the clasts are unaffected by bubble growth and keep the clast density, heat capacity, and thermal conductivity constant. Previous cooling models have also assumed a constant thermal diffusivity, as the interest is in the bulk cooling of the clast (Hort and Gardner, 2000; Capaccioni and Cuccoli, 2005; Wright et al., 2007). The spherically symmetric 1D heat equation is solved to model the spatial and temporal temperature change of the clast:

$$\rho_c c_{p_c} \frac{\partial T}{\partial t} = \frac{k_c}{r^2}\frac{\partial}{\partial r}\left(r^2 \frac{\partial T}{\partial r}\right) \quad (8)$$

where ρ_c is clast density, $c_{p,c}$ is clast heat capacity, r is the radial coordinate, and k_c is thermal conductivity of the clast (See Table 2 for values). The heat equation is solved implicitly with finite difference methods (second order in space and time, unconditionally stable) (Patankar, 1980). A 10^{-2} second timestep is used, and the 1D profile has a 10^{-4} meter resolution. The numerical solution for conduction and convection

is verified against an analytical solution (Eckert and Drake, 1987; Incropera and DeWitt, 1996).

The surface cooling of the clast is modeled by calculating the heat flux. This allows the calculation of the clast temperature as a result of its interaction with the surrounding environment through forced convection and radiation. The surface heat flux is

$$k_c \left(\frac{\partial T}{\partial r}\right)_{r=R} = -q_R - q_c, \quad (9)$$

where

$$q_R = \gamma\left(T_\infty^4 - T_{c_s}^4\right) \quad (10)$$

is the radiative heat flux, and

$$q_c = h\left(T_\infty - T_{c_s}\right) \quad (11)$$

is the convective heat flux, γ is black body emissivity, T_{cs} is surface temperature of the clast, T_∞ is the surrounding gas temperature, and h is the heat transfer coefficient. The heat transfer coefficient,

$$h = \frac{Nu\, k_g}{2r_c}, \quad (12)$$

is calculated using the Nusselt number (Nu), the thermal conductivity of the surrounding gas (k_g), and the clast radius (r_c). The Nusselt number is determined from empirical equations acquired from experiments on spheres (Achenbach, 1978) and small volcanic pyroclasts (Stroberg et al., 2010). The equations are dependent on the particle Reynolds number and Prandtl number. The particle Reynolds number,

$$Re_p = \frac{2\left|\left(v_g - v_c\right)\right| r_c \rho_g}{\mu_g}, \quad (13)$$

is the ratio of inertial forces to viscous forces and is determined by the velocity difference between the clast (v_c) and gas (v_g), clast radius (r_c), gas density (ρ_g), and gas viscosity (μ_g). The Prandtl number,

$$Pr = \frac{c_{p_g}\mu_g}{k_g}, \quad (14)$$

is the ratio of momentum diffusion to thermal diffusion and is dependent on the gas phase, where c_{Pg} is gas heat capacity, μ_g is gas viscosity, and k_g is gas thermal conductivity. For ambient air, Pr is ~ 0.71, which is the value used in the experiments on spheres to find the Nusselt number (Achenbach, 1978). Our simulations include more diverse environments that result in Prandtl numbers varying from approximately 0.3 to 0.9. This variation of the Prandtl number results in a 30–40% difference in Nusselt numbers for the low particle Reynolds number ($Re_p < 2.0 \times 10^5$) and we assume the deviation from Pr = 0.71 for the higher particle Reynolds numbers is similar in magnitude.

For low particle Reynolds number ($Re_p < 2.0 \times 10^5$),

$$Nu = 2 + x Re_p^{1/2} Pr^{1/3}, \quad (15)$$

where x = $\rho_c\left[(2.2 \pm 0.3) \times 10^{-4}\right] + (0.31 \pm 0.04)$, and ρ_c is the density of the volcanic clast (Stroberg et al., 2010). For mid-range particle Reynolds number $2.0 \times 10^5 \leq Re_p \leq 4.0 \times 10^5$,

$$Nu = 473.94 \log\left(Re_p\right) - 5436.4. \quad (16)$$

Table 1
Physical properties.[a]

Parameter	Description	Units
c_P	Heat capacity	J/(kg · K)
P	Pressure	Pa
I	Interphase momentum transfer due to drag	Pa/m^3
T	Temperature	K
u	Velocity	m/s
q	Heat flux	J/(m^2 · s)
α	Volume fraction	
τ	Stress tensor	Pa
ρ	Density	kg/m^3
g	Gravity	m/s^2
δ_{ij}	Kronecker delta operator	
$\bar{H}$	Mean interphase heat transfer	J/(m^3 · s)
F_g	Gas drag	m/s^2
F_s	Particle–particle drag	m/s^2

[a] Subscripts s and g in the equations refer to the solid and gas phase, respectively. i and j refer to spatial dimensions (Dufek et al., 2009).

Eq. (16) is from a fit of the data of Achenbach (1978). For high particle Reynolds number $4.0 \times 10^5 < Re_p < 5.0 \times 10^6$,

$$Nu = 430 + a_1 Re_p + b_1 Re_p^2 + c_1 Re_p^3, \tag{17}$$

where $a_1 = 5 \times 10^{-4}$; $b_1 = 0.25 \times 10^{-9}$; $c_1 = -3.1 \times 10^{-17}$ (Achenbach, 1978). There is an error reported in Achenbach (1978) for a_1; see Appendix A for further details.

2.2.2. Clast viscosity

The melt viscosity is calculated at each grid point along the 1D radial profile of the pyroclast with the Giordano et al. (2008) viscosity model. For the input composition, we use whole rock analysis results of a breadcrust bomb from Tungurahua volcano (Samaniego et al., 2011) and vary initial water concentration. The viscosity profile of individual pyroclasts varies throughout the simulation as a result of the changing temperature from cooling and changing water concentration from bubble growth. Vesicularity and crystal content also influence the absolute viscosity (Kaminski and Jaupart, 1997; Llewellin and Manga, 2005; Caricchi et al., 2007). The presence of crystals increases the viscosity,

which restricts bubble growth. To incorporate the effect that fine-grained crystals (i.e., microlites) have on viscosity, the Einstein–Roscoe correlation is applied. The Einstein–Roscoe correlation is,

$$\mu_{m+c} = \mu_m (1 - R\phi)^{-2.5}, \tag{18}$$

where μ_m is the melt viscosity calculated by the Giordano et al. (2008) model, R = 1.67, ϕ is the volume fraction of crystals, and μ_{m+c} is the new viscosity. This correlation has been found to be consistent with crystal volume fractions less than or equal to 30% (Dobran, 2001). In all the models, crystal volume fraction is assumed to be 30%, which is a reasonable value for breadcrust bombs (Burgisser et al., 2010; Giachetti et al., 2010; Samaniego et al., 2011).

The viscosity model enables the calculation of physical properties that are dependent on melt composition, temperature, and viscosity. One such property is the glass transition temperature, T_g (Giordano et al., 2008). The glass transition temperature is the transition of melt from a relaxed viscous liquid to an unrelaxed glass. It depends on composition and thermal history of the material (Gottsmann et al., 2002; Giordano et al., 2005). The glass transition temperature is higher with faster cooling rates and with decreasing water concentrations (Giordano et al., 2005). As many rinds are glassy and non-vesicular, the glass transition is an important property for rind formation and is coupled with our clast- and micro-scale model. If the clast temperature drops below the calculated glass transition temperature, the bubble growth is terminated and the bubble is frozen in place. The glass transition temperature is calculated in the model as the temperature at which the specific melt composition would have a viscosity of 10^{12} Pa·s (Giordano et al., 2008). The assumption is that the melt has a relaxation timescale of ~15 min and a cooling rate of ~10 K/min. Traditionally, the glass transition viscosity is treated as independent of composition and is found to be around 10^{12} Pa·s for cooling rates on the order of several K/min (Gottsmann et al., 2002; Giordano et al., 2005).

2.3. Micro-scale (bubble growth)

The calculation of bubble growth within a viscous melt (Prousevitch et al., 1993) is used to model the rind thickness of the breadcrust bomb.

Table 2
Clast and bubble properties[a].

Parameter	Symbol	Value	Units	Reference
		Pyroclast parameters		
Density	ρ_c	2400	kg/m^3	
Heat capacity	c_{Pc}	1095	J/(kg · K)	Bacon (1977)
Thermal conductivity	k_c	1.5	W/(m · K)	Clauser and Huenges (1995)
Radius	r	0.1	m	
Initial temperature	T_o	1200	K	
Thermal diffusivity	κ_c	5.71×10^{-7}	m^2/s	Whittington et al. (2009)
Black body emissivity	γ	5.67×10^{-8}	W/(m^2 · K^4)	
Initial glass transition temperature	$T_{g,o}$	818	K	Giordano et al. (2008)[b]
		Bubble parameters		
Melt pressure	p_m	10^5	Pa	
Surface tension	σ	0.35	N/m	Walker and Mullins (1981)
Diffusivity H$_2$O	D	9.0×10^{-11}	m^2/s	Behrens et al. (2004)
Henry's constant	K_h	10^{-11}	Pa^{-1}	Burnham (1975)
Initial conc. H$_2$O	c_o	0.01		
Bubble number density	BND	10^{10}	m^{-3}	Hurwitz and Navon (1994)
Initial bubble pressure	P_o	10^5	Pa	
Initial bubble radius	R_o	0.3	μm	
A priori final bubble radius	R_{final}	1420	μm	
Critical bubble radius	R_{cr}	0.071	μm	
Initial shell radius	S_o	288	μm	
Melt density	ρ_m	2400	kg/m^3	

[a] All values are constant except for the initial values c, R, S, T, T_g, and P, which will change with time.
[b] The initial glass temperature is from Giordano et al. (2008) viscosity model using the composition of a bomb from Tungurahua (Samaniego et al., 2011) and an initial water concentration of 1 wt.%.

Bubble growth is calculated radially along the 1D profile of the pyroclast. Radially, all the bubbles start with the same size and the same porosity of ~10^{-7}%. Using the final radial bubble size distribution, we define the interior boundary of the rind as the point at which the spatial gradient of bubble size is maximized.

The Prousevitch et al. (1993) bubble growth model is isothermal, and water diffusivity and viscosity are held constant. To modify this bubble growth model, the changing temperature and viscosity of the melt calculated on the clast-scale model is coupled to the bubble growth model. We assume the melt surrounding the bubble is in thermal equilibrium with the temperature of the clast-scale model. The water concentration at the bubble–melt boundary is used to calculate the viscosity, as the viscous resistance to bubble growth is strongly controlled by the melt nearest the bubble (Blower et al., 2001). The bubble growth model accounts for growth due to the changing volatile concentration profile, the bubble growth resistance from high viscosities, the changing pressure of the bubble (ambient pressure, surface tension, and dynamic pressure), changes in saturation concentration at the bubble–melt interface, and the growing bubble radius. Bubble growth is most affected by the diffusion rate, viscosity of the melt, surface tension, initial water concentration, ambient pressure, and bubble separation (Prousevitch et al., 1993). We do not consider coalescence, multiple nucleation events, ripening, or irregular spacing of bubbles. We tested our model with results from Prousevitch et al. (1993) and Forestier-Coste et al. (2012) and find good agreement.

In the model, the bubbles are each surrounded by a finite volume of melt that is closely packed in a polygonal matrix (see Prousevitch et al. (1993) for further explanation). For the bubbles to grow, the initial bubble radius must be greater than a critical radius,

$$R_{cr} = \frac{2\sigma}{\frac{c_o^2}{K_h} - p_m}. \tag{19}$$

See Table 2 for explanation of symbols and the corresponding values. This results in a critical radius of 0.071 μm. For all simulations, the initial bubble radius is 0.3 μm with a bubble number density of 10^{10} m^{-3} (Hurwitz and Navon, 1994). The maximum size a bubble can grow,

$$R_{final} = R_o \left[\frac{\rho_m}{\rho_g} \frac{S_o^3 - R_o^3}{R_o^3} \left(c_o - (K_h p_m)^{1/2} \right) + \frac{2\sigma}{R_o p_m} + 1 \right]^{1/3}, \tag{20}$$

is calculated a priori based on the initial bubble radius, shell radius, pressure, and density, as well as constant conditions in Table 2. Eqs (19) and (20) are from Prousevitch et al. (1993). If bubble number density is increased, R_{final} and the time for complete bubble growth will decrease (Prousevitch et al., 1993), which will result in smaller rinds. With this bubble growth model, we can examine how bubble growth is restricted as a result of an increase in viscosity from the cooling of the pyroclast. This allows us to calculate rind thickness and examine its correlation with a pyroclast's cooling history.

2.4. Model compilation

Our simulations explore a range of initial conditions with this multi-scale, coupled model (Table 3) to determine whether transport and thermal history influence the rind thickness. At one-second intervals, the macro-scale model records the velocity of each Lagrangian particle (1000 per simulation) and the interpolated Eulerian gas information around the particle (such as velocity, viscosity, heat capacity, density, and mean-temperature) in a data file. The clast- and pore-scale models are run concurrently, reading in the data from the 1000 Lagrangian particles that are tracked in each macro-scale simulation. The heat loss of each particle is determined with the clast-scale model. Viscosity and glass transition temperature are calculated using the Giordano

et al. (2008) model with the temporally changing temperature from the clast-scale model and the temporally changing water concentration profile from the pore-scale model. The temperature, glass transition temperature, and viscosity are applied to the pore-scale model for bubble growth. If the temperature is less than the glass transition temperature, the bubble growth model is stopped at that radial position and the bubble is frozen in place. Each calculation simulates 450 s of eruptive activity.

We first assess how particle trajectories and transport regimes (i.e., projectile vs. PDC entrained) influence the thermal history and rind development in the clast. To more easily discern how path affects the rind thickness, most of the initial conditions are kept the same for each simulation and transport occurs in two primary scenarios, a buoyant eruptive plume with projectile bombs or a PDC propagating laterally with entrained bombs. Run conditions pertinent to each simulation, PDC 1–6 and Projectile 1–6, are included in Table 3. The initial gas temperature for each transport regime is varied between 900 K, 700 K, and 500 K to approximate conditions in a flow with variable near-vent air entrainment. Variable initial entrainment of cold air cools the current and is likely an important component for PDCs that generate breadcrust bombs (Rader et al., in press). For each initial gas temperature, a dense and dilute current for each transport regime is analyzed (see Table 3). The dense and dilute terms are used in relation to our simulations and are not meant as actual end member values for all eruptions. Runs 1 and 2 have the highest initial gas temperature and have a dense (Run 1) and dilute (Run 2) end member. The naming scheme is the same for both the Projectile and PDC runs. An increase in run number correlates to a decrease in initial gas temperature.

The varying density of the buoyant plumes is coupled to the initial ejection velocities. The initial ejection velocity of the current is based on the assumption that the flow is choked at the vent, and we assume a bomb's initial velocity is the same as the current. The exit velocities for the buoyant eruption with projectiles range from ~135–400 m/s and ejection angles are random. The PDC eruptions all start with an initial pyroclast and gas velocity of 20 m/s. In the first 5 s of the simulation, only the continuum model is run to allow the PDC to propagate down the slope; after 5 s the Lagrangian particles start to be introduced in both the interior of the current and slightly above the current. This is done to give pyroclasts an opportunity to distribute throughout the current. We assume a small background wind field (2 m/s) after deposition, to simulate post-depositional cooling. All 1000 Lagrangian pyroclasts per simulation have an initial magmatic temperature of 1200 K, a radius of 10 cm (a bomb radius is > 3.2 cm), and a density of 2400 kg/m^3. For the pyroclast-scale, the material properties of the clasts are held constant (see Table 2), and 1 wt.% H$_2$O is used as the initial water content for the viscosity and bubble growth model. The pore-scale model has the same initial bubble values for all the simulations (see Table 2 for a list of the constant and initial values). We hold constant initial bubble conditions and many of the clast properties in order to focus on how transport regime and transport properties influence rind thickness and breadcrust bomb morphology.

After thermal history is assessed, we investigate how water content and clast size affect the rind thickness. To determine how initial water concentration influences the rind thickness, all initial parameters and transport histories for Projectile 4 and PDC 3 are the same and only initial water concentration is varied from 0.8, 0.9, 1.0, 1.27, 2.0 and 3.0 wt.% H$_2$O (see section Initial water in Table 3). For the clast size variation study, all initial parameters are the same as model runs Projectile 4 and PDC 3, except the pyroclasts within the macro- and clast-scale models now vary in radius size from 2.5 cm to 50 cm (see section Pyroclast size in Table 3). This will cause different transport paths because of variations in size, and will cause different cooling regimes owing to new conductive cooling length scales and heat transfer coefficients.

Table 3
Initial conditions of simulations.

Model name	Initial gas temp. (K)	Volume fraction of gas	Exit velocity (m/s)	Pyroclast radius (cm)	Initial H$_2$O (wt.%)
		Transport & thermal history			
Projectile 1	900	0.998	139.0	10.0	1.0
Projectile 2	900	0.9999	399.4	10.0	1.0
Projectile 3	700	0.998	137.5	10.0	1.0
Projectile 4	700	0.9999	368.2	10.0	1.0
Projectile 5	500	0.998	135.0	10.0	1.0
Projectile 6	500	0.9999	326.8	10.0	1.0
PDC 1	900	0.6	20.0	10.0	1.0
PDC 2	900	0.8	20.0	10.0	1.0
PDC 3	700	0.6	20.0	10.0	1.0
PDC 4	700	0.8	20.0	10.0	1.0
PDC 5	500	0.6	20.0	10.0	1.0
PDC 6	500	0.8	20.0	10.0	1.0
		Initial water			
Projectile 4a	700	0.9999	368.2	10.0	0.8
Projectile 4b	700	0.9999	368.2	10.0	0.9
Projectile 4c	700	0.9999	368.2	10.0	1.25
Projectile 4d	700	0.9999	368.2	10.0	1.5
Projectile 4e	700	0.9999	368.2	10.0	2.0
Projectile 4f	700	0.9999	368.2	10.0	3.0
PDC 3a	700	0.6	20.0	10.0	0.8
PDC 3b	700	0.6	20.0	10.0	0.9
PDC 3c	700	0.6	20.0	10.0	1.25
PDC 3d	700	0.6	20.0	10.0	1.5
PDC 3e	700	0.6	20.0	10.0	2.0
PDC 3f	700	0.6	20.0	10.0	3.0
		Pyroclast size			
Projectile 7	700	0.9999	368.2	2.5	1.0
Projectile 8	700	0.9999	368.2	5.0	1.0
Projectile 9	700	0.9999	368.2	50.0	1.0
PDC 7	700	0.6	20.0	2.5	1.0
PDC 8	700	0.6	20.0	5.0	1.0
PDC 9	700	0.6	20.0	50.0	1.0

3. Results

The multiphase simulations predict textural and cooling differences in pyroclasts due to different transport paths. Here we discuss separately three issues: 1) the distinct paths experienced by particles under each condition; 2) the role of transport path and thermal environment on the cooling profiles experienced in the different scenarios; and 3) radial bubble variations and rind thicknesses that are preserved in deposited clasts.

3.1. Transport history (macro-scale results)

Particles in the multiphase simulations travel along distinct paths that result in different cooling histories and rind thicknesses. For the buoyant plume eruptions, projectiles mostly travel through cooler ambient air. The pyroclasts exit the hot eruption column within seconds and the remainder of the simulation time experience environments close to that of ambient air (Fig. 3). The denser, low velocity plume eruptions (Projectile 1, 3, and 5) eject clasts that travel a shorter
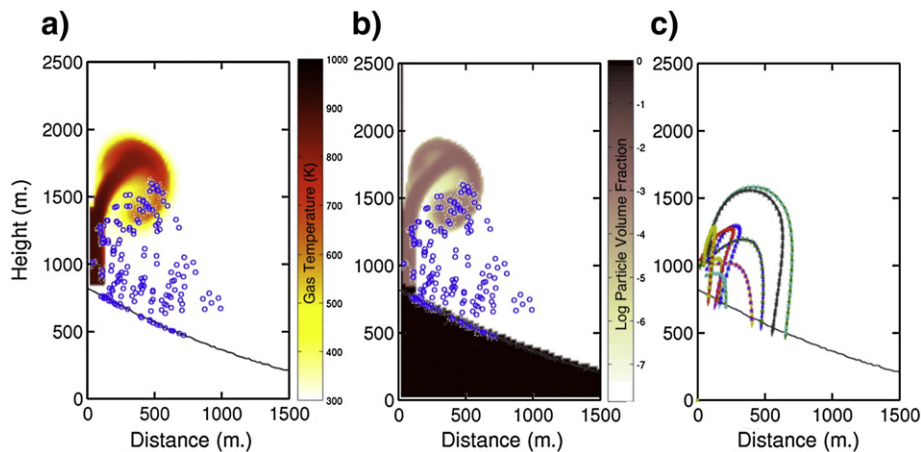

Fig. 3. Projectile 1 model snapshot (not showing total simulation area). a.) Gas temperature contour of the dense Projectile 1 model at 18 s. The initial gas temperature is 900 K. The blue circles are the Lagrangian particles at 18 s. The buoyant plume entrains ambient air and cools along the outer edges. As the figure depicts, the projectiles travel mostly through ambient air. b.) Contour of the volume fraction of particles on a log scale at 18 s and blue circles are the same Lagrangian particles. c.) The complete trajectory path of 10 Lagrangian particles. Note the non-parabolic trajectory for some of the particles.
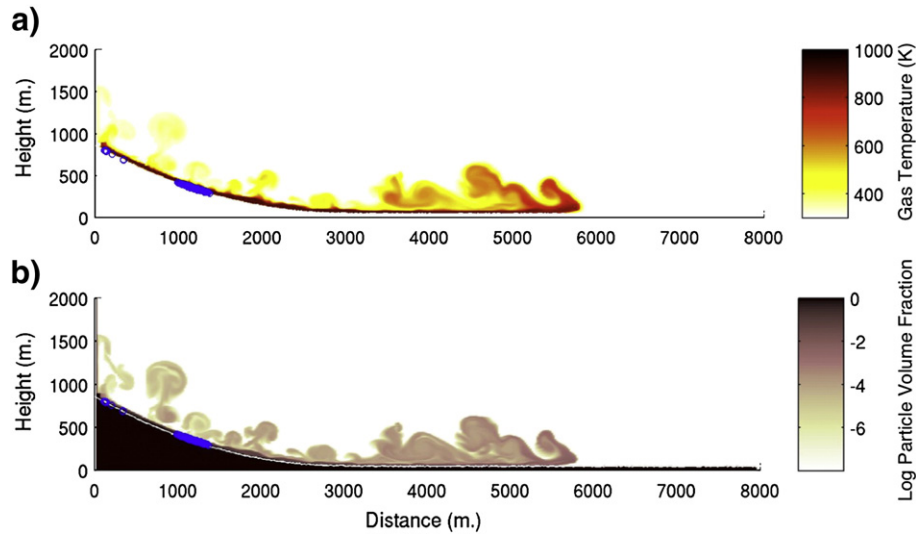
Fig. 4. PDC 1 model snapshot (not showing total simulation area). Lagrangian particles are blue circles. a.) Gas temperature contour for PDC 1 at 68 s. The initial gas temperature is 900 K. Note the cooling of the current by entrainment of ambient air at the top of the current. The bed load region of the current still stays reasonably hot (700–900 K) and is where the larger particles (Lagrangian) are located. b.) Particle volume fraction contour in log scale that depicts higher volume fraction of particles located in the bed load region.

distance by approximately 2 km than those erupted from dilute, high velocity plumes (Projectile 2, 4, and 6). The pyroclast transport time, $\tau_{transport}$, for Projectile 1, 3, and 5 (dense plume eruption) is on average 20 s and for Projectile 2, 4, and 6 (dilute plume eruption) is 33 s. $\tau_{transport}$ is the time the particle is moving and includes the time the particle is in flight and the time it saltates along the ground until it comes to a stop. Some of the pyroclasts do not follow a parabolic trajectory (Fig. 3c) but rather have trajectories that deviate slightly from these parabolic paths as a result of drag between fine particles within the column and recirculating wind currents that develop as the plume ascends. The trajectories of the projectiles are similar to trajectories observed by Vanderkluysen et al. (2012).

The model of PDC results in pyroclasts that travel for longer durations in hot environments compared to projectile pyroclasts. The variation of initial current density results in different run out distances for the large clasts. The pyroclasts in the dense currents (PDC 1, 3, and 5) travel about 1 km further than the pyroclasts in the dilute currents (PDC 2, 4, and 6). For the majority of their transport, the large pyroclasts travel by saltation and through frictional interaction with the body of the current, primarily in the hot, dense bed load region. The bed load region stays the hottest and has the largest volume fraction of particles (Fig. 4). The average $\tau_{transport}$ of the pyroclasts in the dense currents (PDC 1, 3, and 5) is 61 s and 26 s for the dilute currents (PDC 2, 4, and 6).

3.2. Pyroclast cooling history (clast-scale results)

The large thermal gradients between the clast and the atmosphere immediately after eruption lead to rapid cooling at the surface of the clast. This is particularly true for the clasts following projectile trajectories. In the first 60 s, the surfaces of the clasts rapidly cool (Fig. 5) and in general cool more efficiently in buoyant plume simulations. Here we compare the clast temperature to the initial temperature (relative temperature). At 60 s, all 3000 projectile pyroclasts in Fig. 5a cool to a relative temperature of 55–77%, with an average relative temperature of 70%. The clasts that travel dominantly in the core of the plume (and typically land closer to the vent) cool more slowly than those following lower angle trajectories. The lower angle trajectories travel for longer times, deposit furthest from the vent, and the majority of their travel is in the cooler, ambient atmosphere. These clasts have larger particle Reynolds numbers and therefore higher heat transfer coefficients. The surface temperature kink in Fig. 5a (around 40–45 s) is the result of higher conductive heat flux within

the clast compared to the overall surface heat flux. This causes the surface of the clast to heat up again and happens after deposition. Clasts entrained in PDCs typically have more similar transport paths and less variation in their surface temperature than the projectile clasts. An increase in surface temperature variation and cooling corresponds with a decrease in the initial PDC gas temperature (Fig. 5b). At 60 s, the clast surfaces of PDC 1 (900 K initial gas temperature) cool to 85% relative temperature. PDC 3 (700 K initial gas temperature) clast surfaces cool on average to ~82% relative temperature and PDC 5 clasts (500 K initial gas temperature) cool to ~79% relative temperature. PDC 5 does have more variation in surface cooling, covering the entire range of 66–87% relative temperature.

Another useful comparison is the time it takes to cool the pyroclast 200 K throughout specific radial segments of the clast, specifically at the surface and the rind–interior boundary. Although arbitrary, the timescale associated with a 200 K decrease in temperature encompasses the initial fast cooling rates as well as the more gradual temperature changes with diminished thermal gradients. The average cooling times for the projectiles are shorter than the average cooling times for the PDCs. The projectiles' cooling times change with initial density of the current. The dense plumes (Projectile 1, 3, and 5) cool more slowly than the dilute plumes (Projectile 2, 4, and 6). The dilute plume pyroclasts cool more quickly because a dilute current has a higher initial velocity under the choked flow assumption. Higher velocities result in higher particle Reynolds numbers and therefore greater heat transfer. The changes in initial gas temperature make less of a difference on the cooling times (Table 4). For the projectiles, the average cooling rate for the rind to cool 200 K ranges from 400 to 520 K/min. For 10 mm in from the edge of the clast, the average cooling rate is greater than 50 K/min. The time it takes to cool the temperature by 200 K for the PDC pyroclasts varies more with initial gas temperature than with initial current density (Table 4). The average rate to cool the rind 200 K ranges from 80 to 330 K/min, with the rate increasing with decreasing initial gas temperature (or greater initial air entrainment). For 10 mm in from the surface of the clast, the average cooling rate is greater than 30 K/min.

3.3. Rind thickness and bubble growth

3.3.1. Thermal history

The variation in the thermal history of the pyroclast affects its final rind thickness. For the simulations with projectiles, there is little
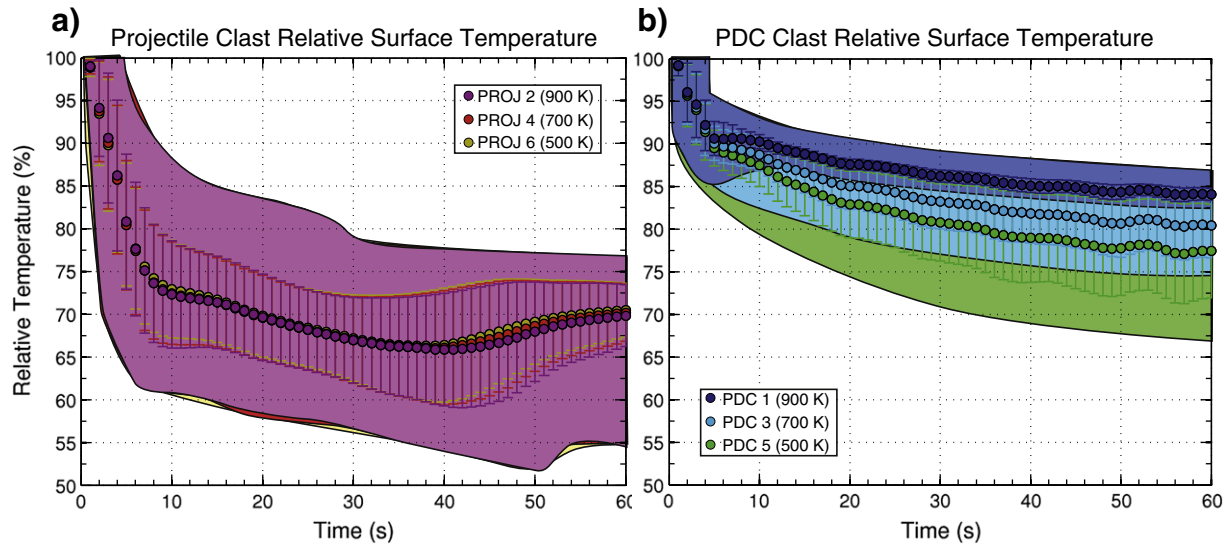
Fig. 5. Relative surface temperature of pyroclasts. The relative surface temperature is the surface temperature of a pyroclast divided by its initial temperature of 1200 K. A relative surface temperature of 65% means the surface has cooled to 780 K. The shaded polygon is the relative temperature area covered by the 1000 particles per simulation for the first 60 s of cooling. The circles are the average of all 1000 particles at each 1-second interval. The error bars are the standard deviation of the average at each 1-second interval. a.) Relative pyroclast surface temperature for the projectile simulations, Projectile 2, 4, and 6. All the projectile pyroclasts experience similar cooling histories, despite varying the initial gas temperature (shown in parentheses in the legend). The kink in the average temperature is the result of surface heat flux being less than the conductive heat flux inside the clast. This occurs after deposition. b.) Relative pyroclast surface temperature for the PDC simulations, PDC 1, 3, and 5. PDC 1 (initial gas temperature = 900 K) has the least variability and smallest amount of cooling for the surface of the clast. As the initial gas temperature decreases (or there is greater entrainment of ambient air), there is more variability in surface temperatures and greater cooling. PDC 5 (initial gas temperature = 500 K) has the greatest amount of surface cooling (~67–87% by 60 s). Even at the lower initial gas temperatures, the PDC pyroclasts do not cool as much as the projectile pyroclasts in the first 60 s.

variation in rind thickness with varying initial gas temperature and more variation as a result of initial current density (Fig. 6 and Table 4). The projectiles from the dilute (faster velocity) eruptions, Projectile 2, 4, and 6, have an average rind thickness of 3.11–3.16 mm over the 900–500 K erupting gas temperature range. The dense (lower velocity) buoyant plumes, Projectile 1, 3, and 5, have pyroclasts with more variation in the average rind thickness, 2.27–2.64 mm, over the 900–500 K gas temperature range. The pyroclasts entrained in the PDC simulations have rinds that are sensitive to the initial gas temperature but not to the initial current density (Fig. 6 and Table 4). At an initial gas temperature of 900 K, the PDC pyroclasts develop rind thicknesses that are on average 1.17 and 1.24 mm for the dilute and dense currents, respectively. As the initial gas temperature decreases (or there is greater air entrainment), the rind thickness on the pyroclasts increases. For both projectile and PDC pyroclasts,

the distribution in rind thickness narrows as the initial erupting gas temperature decreases (Fig. 6d, e, and f).

The rinds on the projectile and PDC pyroclasts also differ in bubble size. The projectile pyroclasts with the thickest rinds have exceptionally small bubbles (bubble radius <10 μm) near the clast edge and increase in bubble size towards the rind–interior boundary (Fig. 7a). The smallest rinds (PDC runs with initial gas temperature of 900 K) have the largest bubbles at the clast edge. Rind thickness and minimum bubbles sizes are correlated; the thickest rind has the smallest bubbles at the edge. The PDC pyroclasts generally have larger bubbles at the edge of the clast than projectile pyroclasts. The minimum bubble radius for the PDC pyroclasts is greater than 10 μm. However, at equivalent rind thicknesses (where rind thicknesses of PDC and projectile clasts intersect in Fig. 6e–f), the PDC and projectile pyroclasts can have similar minimum bubble sizes in the rind. This only occurs for PDC

Table 4
Rind thickness and timescales.

Model	Initial gas temp. (K)	Rind thickness[a] (mm)	$\tau_{transport}$[a] (s)	τ_{rind}[a] (s)	τ_{Tg}[a] (s)	Cool surface 200 K[a] (s)	Cool rind 200 K[a] (s)	Cool outer 10 mm[a] 200 K (s)
				Projectile pyroclasts				
1	900	2.27 ± 0.46	20.80 ± 7.71	28.00 ± 18.02	129.01 ± 49.67	11.61 ± 11.76	27.92 ± 21.07	214.79 ± 29.55
2	900	3.11 ± 0.46	34.62 ± 11.58	21.44 ± 4.23	95.06 ± 48.24	5.86 ± 2.46	29.63 ± 9.99	182.93 ± 17.22
3	700	2.47 ± 0.33	20.25 ± 7.51	27.85 ± 8.68	133.48 ± 25.55	9.46 ± 3.29	31.72 ± 10.49	211.39 ± 10.86
4	700	3.16 ± 0.42	32.45 ± 10.81	22.12 ± 4.70	105.16 ± 45.88	5.40 ± 2.17	27.18 ± 9.30	185.27 ± 15.11
5	500	2.64 ± 0.26	19.49 ± 6.93	29.40 ± 8.76	139.34 ± 16.20	8.05 ± 2.44	32.00 ± 9.64	210.28 ± 7.67
6	500	3.14 ± 0.37	31.35 ± 10.37	23.33 ± 5.10	113.22 ± 42.95	5.24 ± 1.91	28.75 ± 7.43	188.54 ± 12.98
				PDC pyroclasts				
1	900	1.24 ± 0.22	61.99 ± 20.90	122.14 ± 15.44	290.62 ± 40.16	78.58 ± 19.66	137.90 ± 14.49	368.83 ± 26.77
2	900	1.17 ± 0.23	26.64 ± 14.48	91.34 ± 14.12	216.56 ± 44.53	90.21 ± 8.70	106.17 ± 14.40	317.15 ± 31.06
3	700	1.95 ± 0.17	61.98 ± 19.20	39.11 ± 7.51	199.72 ± 12.62	18.24 ± 4.94	49.87 ± 9.80	268.51 ± 4.68
4	700	1.96 ± 0.19	26.63 ± 15.30	55.26 ± 5.27	178.08 ± 17.39	22.40 ± 8.75	68.31 ± 10.12	258.99 ± 7.34
5	500	2.24 ± 0.13	60.38 ± 21.41	28.65 ± 7.19	115.56 ± 29.79	12.36 ± 3.37	38.20 ± 9.62	213.93 ± 9.21
6	500	2.29 ± 0.17	26.88 ± 14.97	35.22 ± 8.74	148.89 ± 4.16	11.36 ± 5.24	46.01 ± 13.10	226.87 ± 4.34

[a] Values are the average result for the 1000 pyroclasts (Lagrangian particles) per model. The number after '±' is the standard deviation of the average.
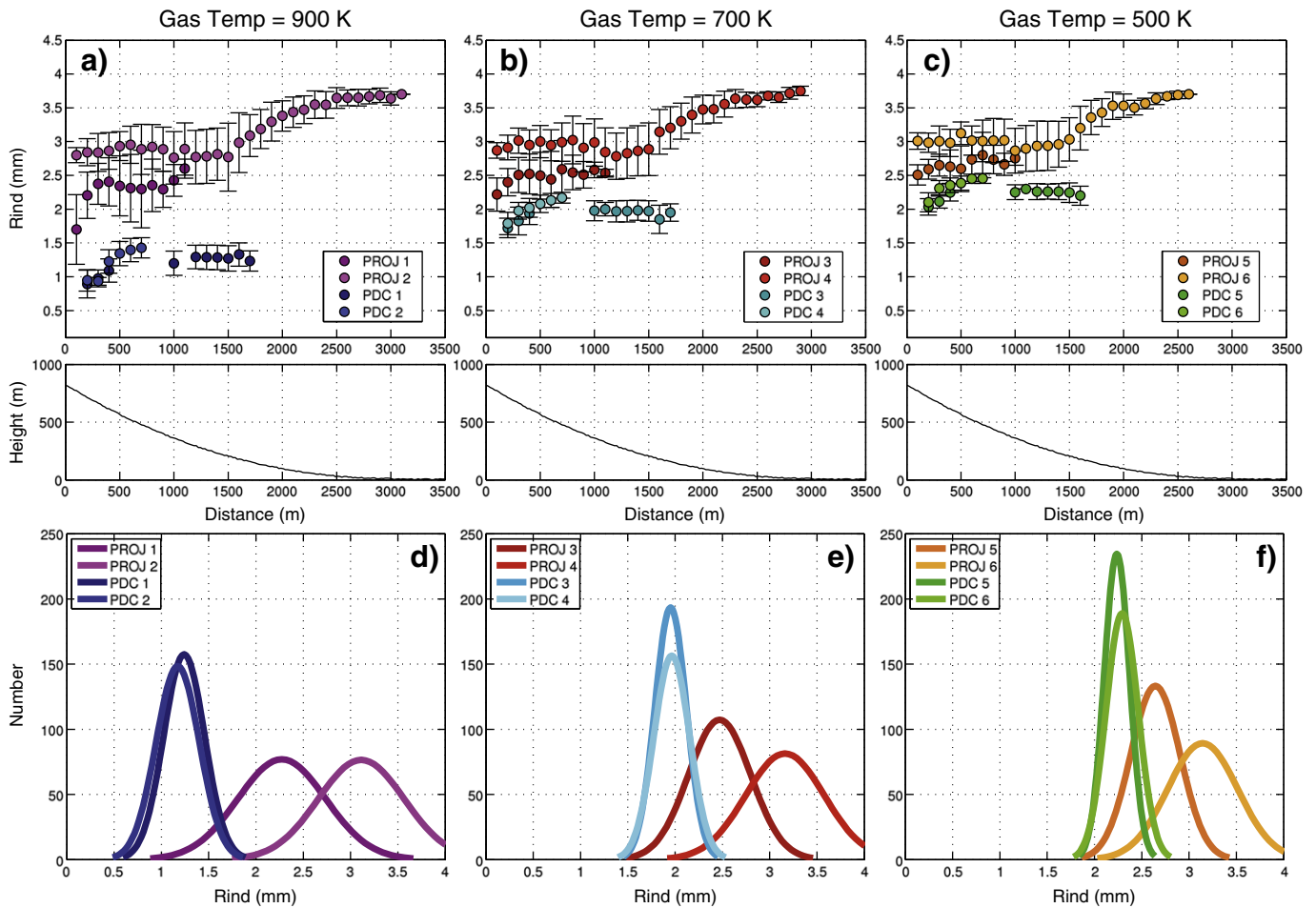
Fig. 6. Rind thickness. a–c.) Binned averages of rind thickness with depositional distance away from the vent for each initial gas temperature (900 K, 700 K, and 500 K). All pyroclasts start with a uniform initial temperature of 1200 K and 1.0 wt.% H_2O. Each point is an average of all particles within the 100-meter horizontal distance bin and the error bars are the standard deviation of all rind thicknesses in that particular bin. The bottom portion of the figure is the topographic profile for the simulation. As gas temperature decreases (greater initial entrainment of air), there is less difference between the rind thickness of projectiles and PDC pyroclasts. Also note the pyroclasts in the dense PDCs travel further than the pyroclasts in the dilute PDCs. The dilute, higher velocity projectile pyroclasts travel the furthest horizontal distance and have the largest rinds. The kink in the projectile rind distribution is an effect of ejection angle. Before the kink, the particles are mostly ejected at higher angles and have lower particle Reynolds and Nusselt numbers than the particles after the kink. d–f.) Distribution of rind thickness for each simulation. Initial gas temperature decreases from left to right. As the initial gas temperature decreases (or as entrainment of air increases), the distribution in rind thickness narrows for all simulations. The distribution of rind thickness illustrates how the rinds of PDC pyroclasts approach similar thicknesses to the rinds of projectile pyroclasts for the 500 K case. It also shows that the initial PDC current density made little difference in rind thickness, but initial current density did affect the rind thickness for the projectile pyroclasts.

runs with initial gas temperatures less than or equal to 700 K. The radial bubble profiles for the PDC pyroclasts show a distinct trend with decreasing initial gas temperature. As the current temperature decreases, the rind increases in thickness and the bubbles at the edge of the clast decrease in size (Fig. 7b).

The radial distribution of bubble sizes in the pyroclasts can also be compared using porosity. The final bubble size, R, and shell of melt around the bubble, S, allows the calculation of porosity at each radial point in the clast using $(R^3/S^3) \cdot 100$. The bubble geometry is closely packed cells that each contains a bubble in the middle and a finite volume of melt surrounding the bubble (Prousevitch et al., 1993). The interior of the bomb will have a final porosity of nearly 100%, because the bubble grows to the equilibrium value determined by Henry's law of water solubility in magmas. At ambient pressure and the initial bubble conditions in Table 2, Henry's law gives a final porosity of 99% (e.g., Prousevitch et al., 1993; Koyaguchi, 2005). The bulk interior porosities are an overestimate since the bubbles are allowed to grow to the final equilibrium state at atmospheric pressure, which does not occur in nature. For example, Wright et al. (2007) has bulk interior porosities between 32 and 71% and Burgisser et al. (2010) has vesicularities in the core between 8 and 44% for Soufriere Hills. However, estimates of porosity with this model should be accurate in the rind where the

distance between bubbles is more pronounced and the spherical shell assumption more robust.

To compare the rind porosities, average rind porosity for each clast is calculated using all the individual bubble porosities in the rind. The PDC runs with an initial gas temperature of 900 K have average rind porosities of 75–95%. The remaining PDC and projectile clasts have average rind porosities between 20 and 65%. The porosity decreases with increasing rind thickness for the PDC and projectile pyroclasts (Fig. 8). The minimum porosity in the rind or the porosity at the edge of the clast for the PDC runs with an initial gas temperature of 900 K is between 30 and 90%. The PDC pyroclasts with initial gas temperature of 700 K have minimum porosities less than 20% and the PDC pyroclasts with an initial gas temperature of 500 K have minimum porosities less than 5%. All the projectile pyroclasts have minimum porosities less than 20% and also decrease to 0% with decreasing initial gas temperature. At equivalent rind thickness, the projectile pyroclasts have similar minimum porosity to PDC pyroclasts, when the initial gas temperature of the PDC is less than or equal to 700 K. There is more overlap in rind thickness and minimum porosity for the PDC and projectile pyroclasts when the projectiles are from the dense buoyant plume (i.e. Projectile 3 and 5).

The cooling history of the pyroclast affects the amount of time it takes to restrict the growth of bubbles within the rind. We define,
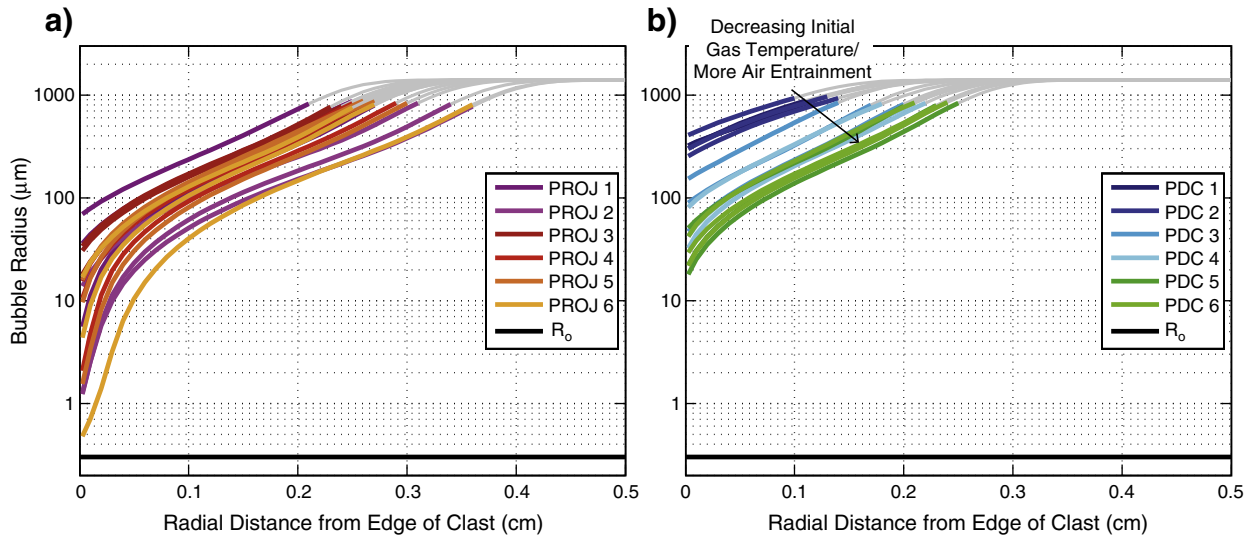
Fig. 7. Bubble radius profiles at the edge of the clast. A small fraction of the particles from each model are plotted. The colored lines are the rinds calculated for the clast. The gray lines show the rest of the bubble sizes in the interior of the clast, which grow to a predetermined size and coalescence is not taken into account. R_o is the initial bubble radius. a.) Bubble radius profiles for the outer 5 mm of the clast for the buoyant plume models. The projectile pyroclasts have a greater size range of bubbles in the rind than the PDC pyroclasts but show no correlation with the initial gas temperature. Some of the projectile pyroclasts have bubbles at the outer edge of the rind that are quickly restricted from growing and therefore close to the size of R_o. b.) Bubble radius profiles for the PDC pyroclast models. The pyroclasts can have bubble sizes that are at least an order magnitude larger than the projectile pyroclasts at the very edge (~0.5 mm). The bubble radius profile within the rind of the PDC pyroclasts shows a distinct trend with initial gas temperature, where the bubble sizes at the edge decrease with decreasing initial gas temperature. The bubble sizes and rind thicknesses of PDC pyroclasts is correlated with the surrounding gas temperature.

τ_{rind}, as the characteristic timescale for the bubble at the rind–interior boundary to reach 99% of its final, restricted size. It is a timescale that is used to quantify the time it takes the low-vesicular rinds to form. Viscous effects in the micro-scale model restrict and terminate bubble growth. The time it takes the melt surrounding the bubble at the rind–interior boundary to cross the calculated glass transition temperature is defined as τ_{Tg}. For all the pyroclasts, τ_{rind} is 2–5 times faster than τ_{Tg}. The calculated glass transition temperature using Giordano et al.

(2008) is based on a slower cooling rate, 10 K/min, than the cooling rates the modeled rinds experience, which exceed 80 K/min. The time-scales for the projectile pyroclasts are correlated with initial current density and relatively poorly correlated with the initial gas temperature. The PDC pyroclasts' τ_{rind} and τ_{Tg} are correlated with initial gas temperature and poorly correlated with current density (Table 4), similar to the rind thickness results.
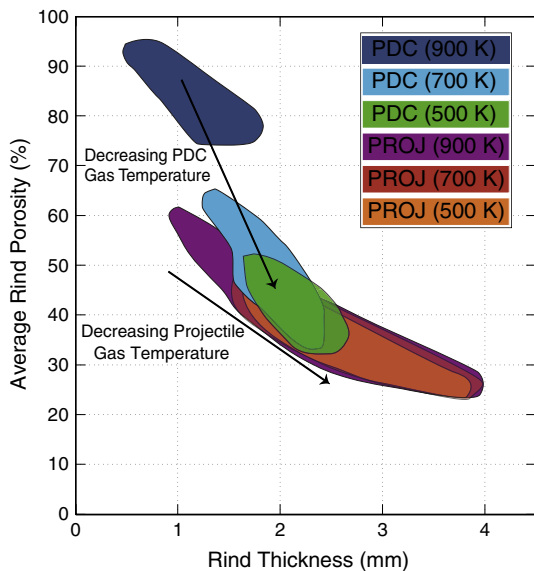

Fig. 8. Average porosity in the rind. Porosity is calculated with the final bubble and shell radius, $(R^3/S^3) \cdot 100$, at 450 s. The average rind porosity is the average of all individual bubble porosities in the rind. As initial gas temperature decreases, the rind thickness increases and the average rind porosity decreases for the PDC pyroclasts. The projectile pyroclasts decrease slightly in average rind porosity with decreasing initial gas temperature. The projectile pyroclasts have the thickest and least vesicular rinds. If there is significant entrainment initially into the PDC, the rind thicknesses and porosities of PDC pyroclasts begin to collapse onto the projectile pyroclast region.
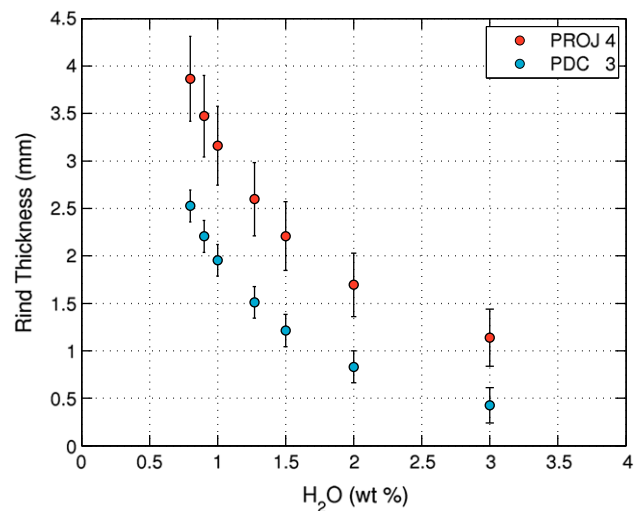
Fig. 9. Rind thickness dependence on initial water and transport path. The comparison uses the thermal history of 1000 particles in the Projectile 4 and PDC 3 simulations, but the initial water concentration is varied. The initial gas temperature is 700 K for these models. Each point is the average rind thickness of 1000 particles and the error bar is the standard deviation for those particles. As initial water concentration is increased, the resultant rind thickness decreases. In the figure, focusing on a rind with a thickness of roughly 1.25 mm shows that the thickness is the result of a PDC pyroclast with 1.5 wt.% H_2O or a projectile pyroclast with 3 wt.% H_2O, thus illustrating how rind thickness is dependent on both water concentration and transport path.

3.3.2. Rind thickness due to water concentration

The initial water concentration and transport path of pyroclasts have a first order impact on rind thickness (Fig. 9). For both PDC 3f and Projectile 4f, the highest water concentration of 3.0 wt.% in the molten pyroclast results in the thinnest rinds with an average thickness of 0.42 mm and 1.14 mm, respectively. The lowest initial water concentration of 0.8 wt.% in the molten pyroclast results in the largest rinds with an average rind thickness of 2.53 mm for PDC 3a pyroclasts and 3.87 mm for Projectile 4a pyroclasts (Fig. 9). Around 0.5 wt.% dense bombs form because the bubbles are unable to grow. As initial water is increased the rind thickness decreases and rind porosity increases along the same trend in Fig. 9. The threshold for when a dense bomb or a vesicular bomb with no rind forms depends on the initial bubble conditions and bomb composition. Transport regime is a factor in rind thickness for all water concentrations. For the lowest initial water concentration, there is relative change of 34.63% in rind thickness between the PDC and projectile pyroclasts and for the highest initial water concentration there is a relative change of 63.16% in rind thickness between the two transport paths.

In addition to variations in rind thickness based on initial water concentration, there is also a difference in the radial bubble size distributions within the rind. The minimum bubble radii in the rind are at the very edge of the clast. For Projectile 4a (0.8 wt.% H_2O), the minimum bubble radius in the rind varies from 0.34 to 17 µm and the minimum bubble radius in the rinds of Projectile 4f (3.0 wt.% H_2O) pyroclasts varies from 17 to 450 µm. For the pyroclasts of PDC 3a (0.8 wt.% H_2O), the minimum bubble radius in the rind varies from 2.3 to 72 µm, and for PDC 3f the minimum bubble radius varies from 390 to 1360 µm. For both PDC and projectile pyroclasts, the 3.0 wt.% H_2O rinds have a larger average bubble size than the 0.8 wt.% H_2O rinds.

3.3.3. Rind thickness due to clast radius

The simulations with varying clast radii result in different particle Reynolds numbers and heat transfer coefficients because of the change in radius. The PDC simulations also result in different paths traveled and environments experienced because of the change in particle radius. The smaller pyroclasts for the PDC case travel the furthest distance, around 3.4 km (Fig. 10d). The distance traveled does not vary significantly for the projectile clasts because the particle Reynolds number is high ($Re_p > 3 \times 10^4$) for all cases, and therefore the drag force on these large clasts

only varies slightly. Both the projectile and PDC pyroclasts show the same trend, whereby cooling is fastest for the smaller clasts. This results in increasing rind thickness with decreasing clast radius (Fig. 10).

4. Discussion

4.1. Thermal history influence on rind thickness and timescales

The transport regime (projectile or PDC) of a pyroclast has a first order influence on the rind thickness. Projectile pyroclasts in general develop thicker and less vesicular rinds than the PDC pyroclasts (Fig. 8). Thicker rinds develop on the high velocity pyroclasts due to high heat fluxes. The high heat fluxes are a result of higher particle Reynolds number and greater temperature differences between the air and clast. The rind thickness of pyroclasts entrained in PDCs depends strongly on the thermal history of the current. The PDC pyroclasts develop thicker and less vesicular rinds as the initial gas temperature decreases. The decrease in initial gas temperature is a proxy for greater entrainment of ambient air during the collapse phase that forms the PDC. A PDC with limited ambient air entrainment retains heat, thus does not maintain enough of a temperature difference between the pyroclast and current to cool the pyroclast fast enough to restrict bubble growth. The thicker rinds are a result of the cooling rate of the pyroclast being faster than the growth rate of the bubbles. Thus the thermal environment (and initial air entrainment) affects the development and thickness of rinds in PDCs.

In all the PDC simulations, the 20 cm diameter clasts are concentrated in the bed load region of the current, which is the hotter part of the current in the simulation. This implies that the pyroclasts are not sampling the entire thermal environment of the PDC with equal fidelity and are biased toward sampling the thermal information from the bed load region. We did not incorporate the entrainment of colder substrate and subsequent cooling of the current from the bed load region. This lack of erosion could bias our currents to hotter conditions (Eichelberger and Koch, 1979; Marti et al., 1991).

A regime diagram that compares transport regime and rind thicknesses (Fig. 11) shows the distinction between the two transport paths and thermal environments. The vertical axis is the rind thickness (mm), L_{rind}, over the conduction length scale (mm), $L_{conduction}$. The conduction length scale (in mm) is calculated using the total
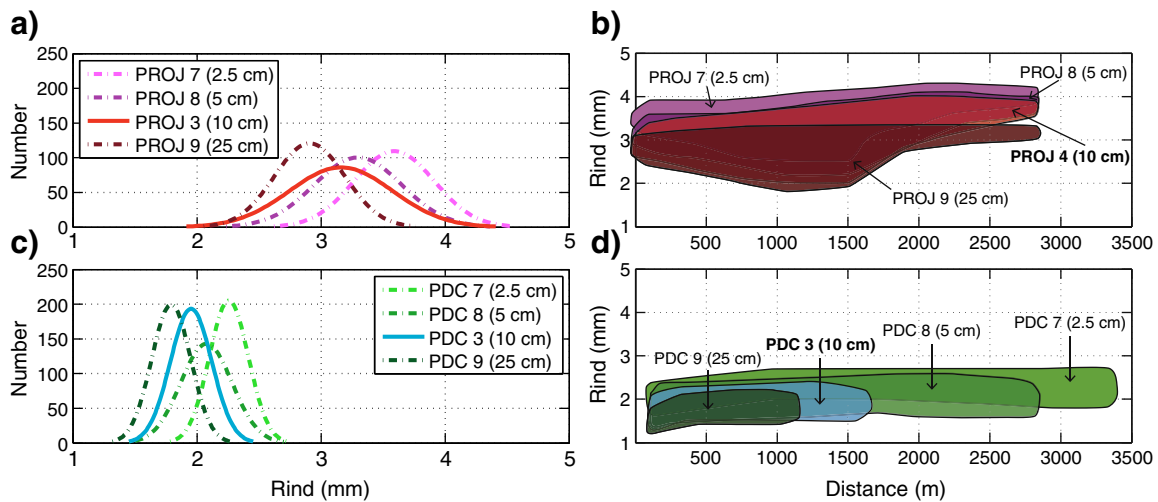

Fig. 10. Variation in rind thickness as a result of clast radius. Both transport paths give the same result, decreasing rind thickness with increasing clast radius. a.) Distribution of rind thickness for projectiles with varying clast radius. b.) Rind thickness versus depositional distance from the vent for projectile pyroclasts of varying radius. The pink (2.5 cm) clasts have the thickest rinds. The magenta (5 cm) and red (10 cm) pyroclasts are the most similar in rind thickness, and the 25 cm pyroclasts have distinctly smaller rinds. c.) Distribution of rind thickness for PDC pyroclasts with varying radius. d.) PDC pyroclast rind thickness versus depositional distance from vent. Note the smallest clasts travel the furthest horizontal distance and have the thickest rinds.
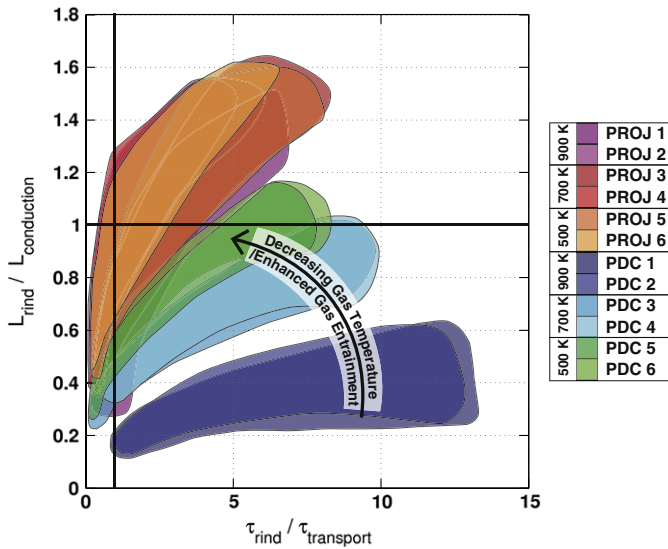
Fig. 11. Regime diagram. As the initial gas temperature decreases the PDC pyroclasts develop thicker rinds and begin to collapse onto the projectile pyroclast area. Most of the PDC pyroclasts fall below 1 on the vertical axis; implying conductive cooling is more important for PDC pyroclast rind formation and heat flux cooling is more critical for projectile pyroclast rind formation. The projectile pyroclast area varies very little with the changing initial gas temperature. This is a result of the quick exit out of the eruptive column into the cool, ambient air environment. There are a few outliers for the projectiles from the general shaded area of each simulation. 99.4% of the projectile pyroclasts fall within their respective shaded areas and 100.0% of the PDC pyroclasts fall in their respective shaded areas. Pyroclasts that are greater than 1 on the horizontal axis still have bubbles growing in the rind after deposition. Even though the bubbles are still growing after deposition, the majority of bubble growth is almost complete before deposition and the growth after deposition is very slow with very little change in size.

travel time of each pyroclast and the constant thermal diffusivity of the pyroclasts, where

$$L_{conduction} = \left(\sqrt{\tau_{transport} \cdot \kappa_c} \right) \cdot 1000. \tag{21}$$

The horizontal axis is τ_{rind} over $\tau_{transport}$. The regime diagram depicts that for some of the projectile and PDC pyroclasts, the conductive cooling during transport is not the determining factor but rather the heat flux from radiative and convective cooling is most significant in determining rind thickness. This occurs for pyroclasts that fall above the value of one on the vertical axis. Above this value, the rind thickness is greater than the length scale that is conductively cooled during the time the pyroclast travels.

On the horizontal axis, the pyroclasts with values greater than one have rinds that are still forming after they have been deposited. Such clasts are common in PDC deposits, but some projectile clasts also fall past one on the horizontal axis. It should be noted; however, that while some bubbles grow in these clasts after deposition, the majority of bubble growth (and rind formation) is during transport, as bubbles grow initially very quickly from diffusion-limited growth and then slowly reach their final size by viscous-limited growth. In the rind, all the bubbles stop growing and do not reach the *a priori* R_{final} (Eq. (20)) because viscosity of the melt surrounding the bubble terminates growth. Field observations suggest that rinds form during transport because some bombs are found abraded with both thick and thin rinds on a single clast. Field observation also indicates that some bombs are plastic at the time of deposition and expand after deposition. Many bombs are found intact in deposits, but in their cool, expanded state they are exceedingly fragile (Walker, 1969, 1982; Wright et al., 2007; Giachetti et al., 2010). The cooling model of Wright et al. (2007)

determine that some of the thinner rinds on the ballistic clasts form before impact but the thicker rinds may have still grown after impact.

The regime diagram illustrates that pyroclasts entrained in PDCs develop rind thicknesses that are dependent on the surrounding gas temperature, which supports the hypothesis that the rind thickness in breadcrust bombs is a useful thermal proxy for the thermal history of PDCs. The diagram shows that with decreasing initial gas temperature, the PDC pyroclasts begin to collapse onto the projectile region (see Fig. 11). With decreasing initial gas temperature (i.e., greater ambient air entrainment), PDC pyroclasts begin to develop thicker rinds due to faster cooling and higher viscosities at the edge of the clast. The faster cooling of a pyroclast restricts bubble growth more quickly and therefore causes τ_{rind} to decrease. All these changes cause the collapse of PDC pyroclasts onto the projectile pyroclast region.

The model developed here and the comparison between timescales, τ_{rind}, τ_{Tg}, and $\tau_{transport}$, for the projectiles and PDC pyroclasts provides insight into the timing of rind formation. In these calculations, τ_{rind} suggests that the first two minutes after eruption is critical for rind formation for this general case of homogeneous and instantaneous nucleation of bubbles with the onset of eruption (Table 4). For colder eruption environments, such as enhanced air entrainment or transport through ambient air, the time for the rind to form is less than a minute. The pyroclasts transported in a hot PDC (initial gas temperature 900 K) take one to two minutes longer to cool, which causes thinner rinds to form. The rinds of pyroclasts from hot PDCs have larger average bubble sizes than the other pyroclast rinds. For initial gas temperatures of 900 and 700 K, the PDC pyroclasts with rind thicknesses similar to projectile pyroclasts are generally more vesicular than the projectile rinds (Fig. 8). In the field, it may be possible to distinguish a PDC and projectile pyroclast from each other not only by rind thickness but also by the vesicularity of the rind.

4.2. Physical insights and assumptions from the model

An interesting detail that emerges from the coupled model is that viscous effects ultimately limit bubble growth in the rinds of breadcrust bombs. The coupled model should develop thicker rinds if the initial viscosity is increased either by using more silicic compositions or having a higher crystal volume fraction. The temperature range that bubble growth is terminated is higher than the glass transition temperature that is calculated under the cooling rate assumption of 10 K/min (Giordano et al., 2005, 2008). Kaminski and Jaupart (1997) found a similar result where the rinds on pumice formed from viscous quenching and before crossing the implied glass transition temperature. The initial glass transition temperature for our model is about 820 K (see Table 2), but it fluctuates in our model because of water loss through diffusion into bubbles. The assumption of a 10 K/min cooling rate for the glass transition temperature may not be realistic because the calculated cooling rate for all modeled rinds is greater than 80 K/min and often much faster. The viscous restriction of bubble growth at high cooling rates may be at the glass transition temperature applicable for higher cooling rates (>10 K/min), although this is difficult to access with the current model for glass transition with these compositions (Giordano et al., 2008). Therefore, this result suggests that faster cooling rates (and higher implied glass transition temperatures) may be required to predict final rind thicknesses if explicit bubble growth is not considered.

When constructing this model, several simplifying assumptions were made and here we evaluate the impact of these assumptions on cooling rate and rind formation. The assumption that particles are spherical and isotropic results in slower cooling compared to more jagged or oblong clasts because of their lower surface area. Experiments on particles over lower Reynolds numbers, $1.1 \times 10^4 < Re < 5.2 \times 10^4$, found that the cooling of spheroids (aspect ratios < 0.67) increased the Nusselt number by 40% or less compared to spherical clasts (Zheng and List, 1996). We also used the black body emissivity for the radiative heat transfer and are therefore calculating the maximum radiative heat

transfer. Radiative heat transfer is only important for the initial few seconds when there is a large temperature difference between the surface and surrounding air. Therefore, the black body assumption likely does not have a large effect on the cooling history. We do not examine the spinning and potentially faster cooling of the pyroclasts or the abrasion of the clasts as they travel, which might be important to the cooling history of individual clasts (Vanderkluysen et al., 2012). The same experiments of Zheng and List (1996) found that spinning between 5 and 22 Hz made only a small difference in the total Nusselt number and this difference was within their experimental error.

An improvement of our model compared to previous efforts is the ability to take into account the differential velocity between the moving particle and the moving current of hot gases with heterogeneous temperatures. Furthermore, we use the correct empirical Nusselt number from the experiments of Achenbach (1978) to calculate the heat transfer coefficient. As reported in the Appendix A, the Nusselt number from the Achenbach (1978) empirical equation for $Re_p > 4.0 \times 10^5$ is up to six times larger than their experimental results and the Nusselt value we calculate. The result of this correction is a lower Nusselt number and slower cooling of pyroclasts at high particle Reynolds number ($Re_p > 4.0 \times 10^5$). Consequently, though we have simplified the problem to better understand the sensitivity of the cooling to physical parameters, the simplification

of assuming a sphere results in less than a 40% lower Nusselt number compared to non-spherical clasts. By comparison, our correction to the empirical equation for convective cooling (Achenbach, 1978) yields a Nusselt number that is up to six times smaller than the reported value for high Reynolds numbers.

4.3. Rind thickness as a result of initial water

Similar to previous studies (Hort and Gardner, 2000; Wright et al., 2007), the rind thickness is found to decrease with increasing water concentration for both projectile and PDC models (Fig. 9). This trend has been noted in ballistic breadcrust bombs at Guagua Pichincha where increasing rind thickness correlates to decreasing water content trapped in the glass of the rinds (Wright et al., 2007). Breadcrust bombs at Guagua Pichincha are described as "finely breadcrusted" and "thickly breadcrusted". The finely breadcrusted bombs have rinds less than 3 mm, 1.4–3.1 wt.% H_2O, and 30–54% vesicularity. The thickly breadcrusted bombs have rinds greater than 3 mm, 1.0–1.3 wt.% H_2O, and 0–13% vesicularity (Wright et al., 2007). The small rind thickness and larger average bubble size in the rind for the 3.0 wt.% rinds (Projectile 4f) could be described as finely breadcrusted and the 0.8 wt.% rinds (Projectile 4a and PDC 3a) could be classified as coarsely breadcrusted.
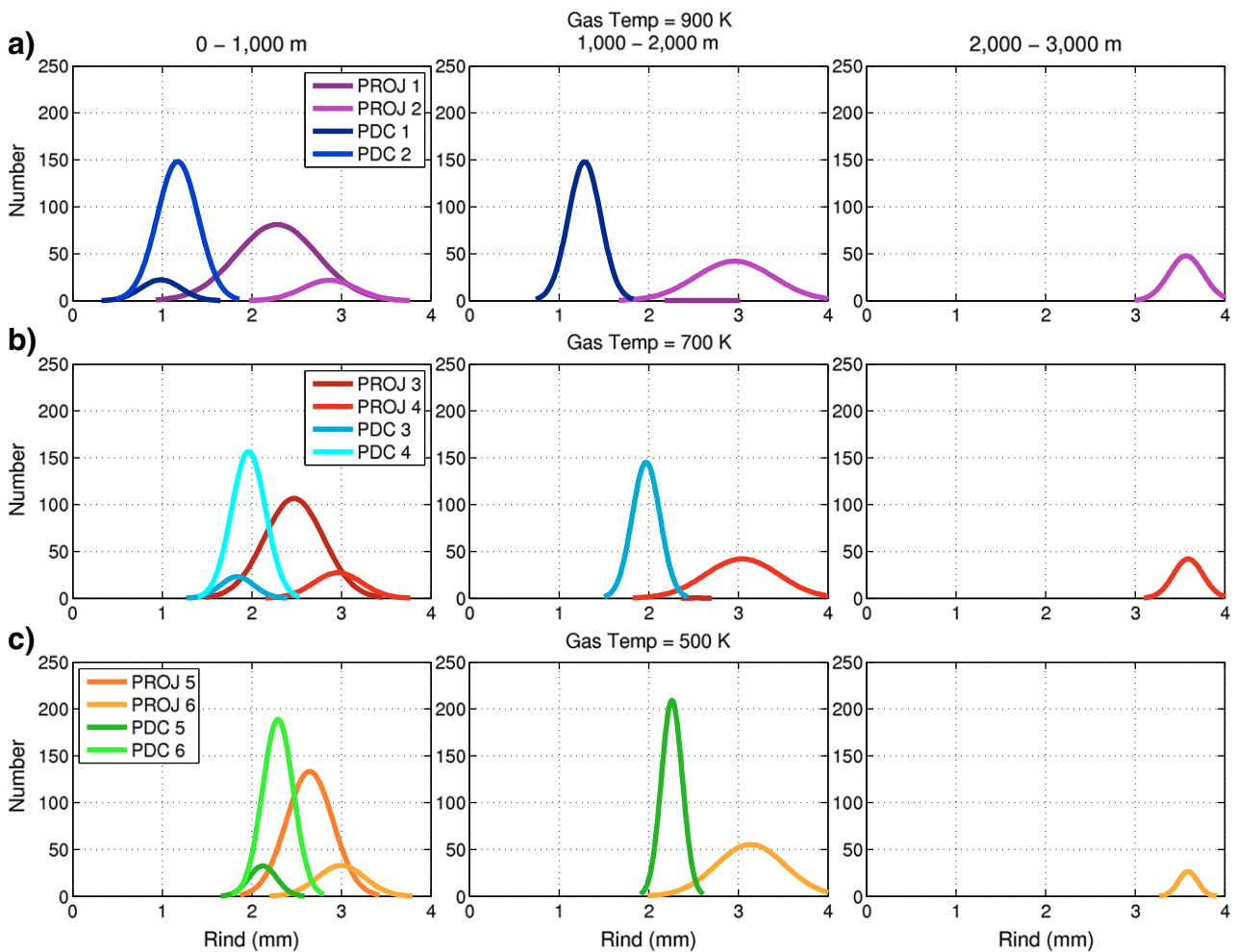

Fig. 12. Distribution of rind thickness based on distance away from vent. From left to right are the binned deposit distances of 0–1000 m, 1000–2000 m, and 2000–3000 m. a.) Distribution of rind thickness for an initial gas temperature of 900 K. b.) Distribution of rind thickness for an initial gas temperature of 700 K. Notice the increase in rind thickness for the PDC pyroclasts. c.) Distribution of rind thickness for an initial gas temperature of 500 K gas. The PDC pyroclast rind thickness distribution now overlaps more with the projectile rind thickness distribution. As the initial gas temperature is decreased (or the transport temperature is more homogeneous and similar to ambient air), the distribution in rind thickness becomes tighter for all the simulations. For the 2000–3000 m box at all gas temperatures, the high velocity projectiles have the mode with the largest rind thickness.

In our simulations, the thickest rinds develop around 1 wt.% H_2O, which parallels the findings of Wright et al. (2007). Some of the reasons rinds get thicker with decreasing water concentration is greater bubble nucleation delay (Wright et al., 2007), slower bubble growth rates, or slower flux of water. In our model it is the last two. With lower water concentration, the viscosity will be higher and will more effectively restrict and slow bubble growth. Lower water concentrations have slower growth rates and do not generate as steep of a concentration gradient as higher water contents. Therefore, the flux of water is slower for lower water concentrations. This results in slower growth rates (Prousevitch et al., 1993). A comparison of the two cooling schemes with variable water concentration reveals that the initial water concentration and transport regime are both first order influences on rind thickness. Modeling the formation of rind thickness using a better-constrained initial water concentration will likely provide clues to the thermal history of the clast.

4.4. Pyroclasts as a thermal proxy for PDCs

The model developed here provides a guideline for the interpretation of textural features of pyroclasts. As Fig. 12 illustrates, pyroclasts ejected into material with higher gas temperatures have a wider variance of rind thicknesses once deposited. A small distribution in rind thickness is the result of a cooler current or a homogeneous transport history. A distal projectile pyroclast should have a thicker rind than the majority of the proximal projectiles. Analysis of water content in the rinds should also be considered when comparing different projectile distances, as different rind thicknesses may also result from different fragmentation depths (Wright et al., 2007). If rind thicknesses are similar at one depositional area but the morphology of the clasts (i.e., radial bubble size distribution) are different, this may indicate variations in transport mechanisms or initial water concentrations. The radial bubble size distribution provides key information about a clast's thermal history and initial water concentration. In our model, generally a pyroclast that has a more vesicular and thinner rind indicates transport in a PDC, an abnormally hot thermal history, or high initial water concentration. The thinner, more vesicular rinds match the description of finely breadcrusted bombs from both Wright et al. (2007) and Giachetti et al. (2010) even though the descriptions for the Guagua Pichincha breadcrust bombs are for ballistic bombs. A coarsely breadcrusted bomb in our model is the result of low water concentration, low environment temperatures, or high transport velocities.

5. Conclusions

Breadcrust bombs are deposited not only as projectiles but are commonly found in PDC deposits. Our results show that systematic textural variation will develop in bombs transported by different means. The thickness and texture of the rinds in breadcrust bombs reflect the influence of transport regime, transport properties, and clast properties. These affect the cooling rate, viscosity, and bubble growth rate that ultimately control the rind thickness. The simulations also provide insight into the timing of rind formation. For the general initial conditions postulated here, it takes < 2 min for the rinds to form. The integrated model compares how a rind develops in a pyroclast that is transported by the two end members of transportation, projectiles out of the buoyant plume and entrainment in PDCs. For clasts entrained in a hot PDC (gas temperature > 900 K), the developed rind thickness is noticeably thinner than the rinds of projectile pyroclasts. Clasts entrained in colder PDCs produce similar rind thicknesses to projectile pyroclasts. Thickly breadcrusted bombs found in the field are the result of fast cooling rates (low surrounding gas temperatures or high velocities) and slow bubble growth rates (low initial water concentration or high viscosities due to quick cooling). A finely breadcrusted
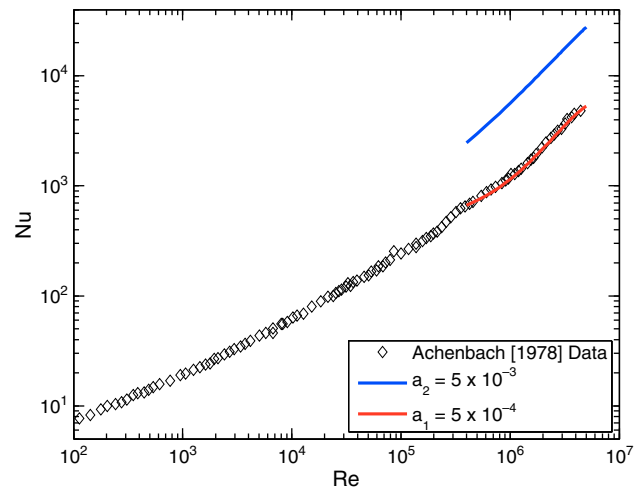

Fig. A1. Comparison of Eq. (17) using $a_2 = 5\text{x}^{-3}$ as reported in Achenbach (1978) and $a_1 = 5\text{x}^{-4}$ with the replotted experimental data from Achenbach (1978).

bomb is indicative of a hot thermal environment, slow transport velocity, or high initial water concentration.

In summary, breadcrust bomb rind thickness and porosity provide insight into the individual cooling history of pyroclasts. Under most conditions, the distribution of porosity and rind thickness for PDC and projectile clasts are distinct. The textural variations in PDC pyroclasts are typically indicative of variable amounts of current cooling from entrainment and initial water contents.

Appendix A

The empirical equation to calculate the Nusselt number for Reynolds numbers greater than 4×10^5 is found through experiments on spheres (Achenbach, 1978). The value of coefficient, a, for that empirical equation in Achenbach (1978) does not match their data. The value for a is stated as 5×10^{-3} in Achenbach (1978), and we will refer to it from now on as a_2. Our own polynomial fit of the experimental data reveals that the correct coefficient value is $a_1 = 5 \times 10^{-4}$ (See Fig. A1). The use of coefficient a_2 results in over 5 times larger Nusselt numbers than were found experimentally for $Re > 4 \times 10^5$. We use the value of a_2 reported by Achenbach (1978) and the value of a_1 in our coupled model to compare the impact of a_2 on cooling calculations. We will focus here on the Projectile 1 model. With a_2, the heat transfer coefficient is up to 6 times larger than the heat transfer coefficient for $a_1 = 5 \times 10^{-4}$. The surface temperature when using a_2 is up to 250 K lower than the surface temperature for a_1 in the first 30 s. The rapid cooling changes the time it takes the rind to form or the time it takes a pyroclast to reach the glass transition temperature by a factor of 2. For example, the average τ_{rind} for Projectile 1 is 28.00 s but with a_2 it is 15.73 s. The average τ_{Tg} for Projectile 1 is 129.01 s but with a_2 it is 64.89 s. The use of a_2 increased the average rind thickness by approximately 1 mm.

References

Achenbach, E., 1978. Heat transfer from spheres up to $Re = 6 \times 10^6$. Proc. Sixth Int. Heat Transfer Conf. 5, 341–346.

Anderson, S.W., Krinsley, D.H., Fink, J.H., 1994. Criteria for recognition of constructional silicic lava flow surfaces. Earth Surf. Process. Landf. 19, 531–541.

Bacon, C.R., 1977. High temperature heat content and heat capacity of silicate glasses: experimental determination and a model for calculation. Am. J. Sci. 277, 109–135.

Behrens, H., Zhang, Y., Xu, Z., 2004. H2O diffusion in dacitic and andesitic melts. Geochim. Cosmochim. Acta 68, 5139–5150.

Blower, J.D., Mader, H.M., Wilson, S., 2001. Coupling of viscous and diffusive controls on bubble growth during explosive volcanic eruptions. Earth Planet. Sci. Lett. 193, 47–56.

Branney, M.J., Kokelaar, B.P., 2002. Pyroclastic density currents and the sedimentation of ignimbrites. Memoirs Geological Society, London.

Burgisser, A., Bergantz, G.W., Breidenthal, R.E., 2005. Addressing complexity in laboratory experiments: the scaling of dilute multiphase flows in magmatic systems. J. Volcanol. Geotherm. Res. 141, 245–265.

Burgisser, A., Poussineau, S., Arbaret, L., Druitt, T.H., Giachetti, T., Bourdier, J.-L., 2010. Pre-explosive conduit conditions of the 1997 Vulcanian explosions at Soufrière Hills Volcano, Montserrat: I. Pressure and vesicularity distributions. J. Volcanol. Geotherm. Res. 194, 27–41.

Burnham, C.W., 1975. Water and magmas; a mixing model. Geochim. Cosmochim. Acta 39, 1077–1084.

Bursik, M.I., Woods, A.W., 1996. The dynamics and thermodynamics of large ash flows. Bull. Volcanol. 58, 175–193.

Calder, E.S., Sparks, R., Gardeweg, M.C., 2000. Erosion, transport and segregation of pumice and lithic clasts in pyroclastic flows inferred from ignimbrite at Lascar Volcano, Chile. J. Volcanol. Geotherm. Res. 104, 201–235.

Capaccioni, B., Cuccoli, F., 2005. Spatter and welded air fall deposits generated by fire-fountaining eruptions: cooling of pyroclasts during transport and deposition. J. Volcanol. Geotherm. Res. 145, 263–280.

Caricchi, L., Burlini, L., Ulmer, P., Gerya, T., Vassalli, M., Papale, P., 2007. Non-Newtonian rheology of crystal-bearing magmas and implications for magma ascent dynamics. Earth Planet. Sci. Lett. 264, 402–419.

Clarke, A.B., Neri, A., Voight, B., Macedonio, G., Druitt, T.H., 2002. Computational modelling of the transient dynamics of the August 1997 Vulcanian explosions at Soufriere Hills Volcano, Montserrat: influence of initial conduit conditions on near-vent pyroclastic dispersal. Geol. Soc. Lond. Mem. 21, 319–348.

Clauser, C., Huenges, E., 1995. Thermal conductivity of rocks and minerals. AGU Ref. Shelf 3, 105–126.

Dobran, F., 2001. Volcanic Processes: Mechanisms in Material Transport. Kluwer Academic/Plenum Publishers, Norwell, Mass.

Douillet, G.A., Tsang-Hin-Sun, È., Kueppers, U., Letort, J., Pacheco, D.A., Goldstein, F., Aulock, F., Lavallée, Y., Hanson, J.B., Bustillos, J., Robin, C., Ramón, P., Hall, M., Dingwell, D.B., 2013. Sedimentology and geomorphology of the deposits from the August 2006 pyroclastic density currents at Tungurahua volcano, Ecuador. Bull. Volcanol. 75, 765.

Dufek, J., Bergantz, G.W., 2007a. Suspended load and bed-load transport of particle-laden gravity currents: the role of particle–bed interaction. Theor. Comput. Fluid Dyn. 21, 119–145.

Dufek, J., Bergantz, G.W., 2007b. Dynamics and deposits generated by the Kos Plateau Tuff eruption: controls of basal particle loss on pyroclastic flow transport. Geochem. Geophys. Geosyst. 8.

Dufek, J., Manga, M., 2008. In situ production of ash in pyroclastic flows. J. Geophys. Res. Solid Earth 1978–2012, 113.

Dufek, J., Wexler, J., Manga, M., 2009. Transport capacity of pyroclastic density currents: experiments and models of substrate-flow interaction. J. Geophys. Res. Solid Earth 1978–2012, 114.

Dufek, J., Manga, M., Patel, A., 2012. Granular disruption during explosive volcanic eruptions. Nat. Geosci. 5, 561–564.

Eckert, E.R.G., Drake, R.M., 1987. Analysis of heat and mass transfer. Hemisphere Pub. Corp, Washington.

Eichelberger, J.C., Koch, F.G., 1979. Lithic fragments in the Bandelier Tuff, Jemez Mountains, New Mexico. J. Volcanol. Geotherm. Res. 5, 115–134.

Forestier-Coste, L., Mancini, S., Burgisser, A., James, F., 2012. Numerical resolution of a mono-disperse model of bubble growth in magmas. Appl. Math. Model. 36, 5936–5951.

Giachetti, T., Druitt, T., Burgisser, A., Arbaret, L., Galven, C., 2010. Bubble nucleation, growth and coalescence during the 1997 Vulcanian explosions of Soufrière Hills Volcano, Montserrat. J. Volcanol. Geotherm. Res. 193, 215–231.

Giordano, D., Nichols, A., Dingwell, D.B., 2005. Glass transition temperatures of natural hydrous melts: a relationship with shear viscosity and implications for the welding process. J. Volcanol. Geotherm. Res. 142, 105–118.

Giordano, D., Russell, J.K., Dingwell, D.B., 2008. Viscosity of magmatic liquids: a model. Earth Planet. Sci. Lett. 271, 123–134.

Gottsmann, J., Giordano, D., Dingwell, D.B., 2002. Predicting shear viscosity during volcanic processes at the glass transition: a calorimetric calibration. Earth Planet. Sci. Lett. 198, 417–427.

Hall, M., Mothes, P., 2008. The rhyolitic–andesitic eruptive history of Cotopaxi volcano, Ecuador. Bull. Volcanol. 70, 675–702.

Hall, M.L., Robin, C., Beate, B., Mothes, P., Monzier, M., 1999. Tungurahua Volcano, Ecuador: structure, eruptive history and hazards. J. Volcanol. Geotherm. Res. 91, 1–21.

Hallworth, M.A., Phillips, J.C., Huppert, H.E., Sparks, R.S.J., 1993. Entrainment in turbulent gravity currents. Nature 362, 829–831.

Hoblitt, R.P., Harmon, R.S., 1993. Bimodal density distribution of cryptodome dacite from the 1980 eruption of Mount St. Helens, Washington. Bull. Volcanol. 55, 421–437.

Hort, M., Gardner, J., 2000. Constraints on cooling and degassing of pumice during Plinian volcanic eruptions based on model calculations. J. Geophys. Res. 105, 25981–26001.

Hurwitz, S., Navon, O., 1994. Bubble nucleation in rhyolitic melts: experiments at high pressure, temperature, and water content. Earth Planet. Sci. Lett. 122, 267–280.

Incropera, F.P., DeWitt, D.P., 1996. Introduction to Heat Transfer, 3rd ed. Wiley, New York.

Kaminski, É., Jaupart, C., 1997. Expansion and quenching of vesicular magma fragments in Plinian eruptions. J. Geophys. Res. 102, 12187–12203.

Koyaguchi, T., 2005. An analytical study for 1-dimensional steady flow in volcanic conduits. J. Volcanol. Geotherm. Res. 143, 29–52.

Le Pennec, J.-L., Jaya, D., Samaniego, P., Ramon, P., Moreno Yánez, S., Egred, J., Van Der Plicht, J., 2008. The AD 1300–1700 eruptive periods at Tungurahua volcano, Ecuador, revealed by historical narratives, stratigraphy and radiocarbon dating. J. Volcanol. Geotherm. Res. 176, 70–81.

Llewellin, E.W., Manga, M., 2005. Bubble suspension rheology and implications for conduit flow. J. Volcanol. Geotherm. Res. 143, 205–217.

Marti, J., Diez Gil, J.L., Ortiz, R., 1991. Conduction model for the thermal influence of lithic clasts in mixtures of hot gases and ejecta. J. Geophys. Res. 96, 21879–21885.

Maxey, M.R., Riley, J.J., 1983. Equation of motion for a small rigid sphere in a nonuniform flow. Phys. Fluids 26, 883–889.

Moore, J.G., Melson, W.G., 1969. Nuees ardentes of the 1968 eruption of Mayon volcano, Philippines. Bull. Volcanol. 33, 600–620.

Morrissey, M.M., Mastin, L.G., 2002. Vulcanian Eruptions. In: Sigurdsson, H. (Ed.), Encyclopedia of Volcanoes. Academic Press, San Diego, pp. 463–475.

Neri, A., Ongaro, T.E., Macedonio, G., Gidaspow, D., 2003. Multiparticle simulation of collapsing volcanic columns and pyroclastic flow. J. Geophys. Res. 108, 2202.

Patankar, S.V., 1980. Numerical Heat Transfer and Fluid Flow. Hemisphere Pub. Corp, Washington.

Pistolesi, M., Rosi, M., Cioni, R., Cashman, K.V., Rossotti, A., Aguilera, E., 2011. Physical volcanology of the post-twelfth-century activity at Cotopaxi volcano, Ecuador: behavior of an andesitic central volcano. Geol. Soc. Am. Bull. 123, 1193–1215.

Prousevitch, A.A., Sahagian, D.L., Anderson, A.T., 1993. Dynamics of diffusive bubble growth in magmas: isothermal case. J. Geophys. Res. 98, 22283–22307.

Proussevitch, A.A., Sahagian, D.L., 1996. Dynamics of coupled diffusive and decompressive bubble growth in magmatic systems. J. Geophys. Res. 101, 17447–17455.

Rader, E., Geist, D., Geissman, J., Dufek, J., Harpp, K., 2014. Hot clasts and cold blasts: Thermal heterogeneity in boiling-over pyroclastic density currents. In: Ort, M.H., Porreca, M., Geissman, J.W. (Eds.), The Use of Palaeomagnetism and Rock Magnetism to Understand Volcanic Processes. Geological Society, London, Special Publications, 396 (in press).

Samaniego, P., Le Pennec, J.-L., Robin, C., Hidalgo, S., 2011. Petrological analysis of the pre-eruptive magmatic process prior to the 2006 explosive eruptions at Tungurahua volcano (Ecuador). J. Volcanol. Geotherm. Res. 199, 69–84.

Scott, A.C., Sparks, R.S.J., Bull, I.D., Knicker, H., Evershed, R.P., 2008. Temperature proxy data and their significance for the understanding of pyroclastic density currents. Geol. 36, 143–146.

Sparks, R., 1978. The dynamics of bubble formation and growth in magmas: a review and analysis. J. Volcanol. Geotherm. Res. 3, 1–37.

Sparks, R., 1986. The dimensions and dynamics of volcanic eruption columns. Bull. Volcanol. 48, 3–15.

Stroberg, T.W., Manga, M., Dufek, J., 2010. Heat transfer coefficients of natural volcanic clasts. J. Volcanol. Geotherm. Res. 194, 214–219.

Syamlal, M., Rogers, W., O'Brien, T.J., 1993. MFIX Documentation: Theory Guide. Technical Note, DOE/METC-94/1004, NTIS/DE94000087. National Technical Information Service, Springfield, VA.

Tait, S., Thomas, R., Gardner, J., Jaupart, C., 1998. Constraints on cooling rates and permeabilities of pumice in an explosive eruption jet from colour and magnetic mineralogy. J. Volcanol. Geotherm. Res. 86, 79–91.

Thomas, R., Sparks, R., 1992. Cooling of tephra during fallout from eruption columns. Bull. Volcanol. 54, 542–553.

Vanderkluysen, L., Harris, A.J.L., Kelfoun, K., Bonadonna, C., Ripepe, M., 2012. Bombs behaving badly: unexpected trajectories and cooling of volcanic projectiles. Bull. Volcanol. 74, 1849–1858.

Walker, D., Mullins Jr., O., 1981. Surface tension of natural silicate melts from 1,200–1,500C and implications for melt structure. Contrib. Mineral. Petrol. 76, 455–462.

Walker, G., 1969. The breaking of magma. Geol. Mag. 106, 166–173.

Walker, G., 1982. Eruptions of andesitic volcanoes. In: Thorpe, R.S. (Ed.), Andesites: Orogenic Andesites and Related Rocks. Wiley, New York, pp. 403–413.

Whittington, A.G., Hofmeister, A.M., Nabelek, P.I., 2009. Temperature-dependent thermal diffusivity of the Earth's crust and implications for magmatism. Nature 458, 319–321.

Wilson, C.J.N., Houghton, B.F., 2002. Pyroclast Transport and Deposition. In: Sigurdsson, H. (Ed.), Encyclopedia of Volcanoes. Academic Press, San Diego, pp. 545–554.

Wright, H.M.N., Cashman, K.V., Rosi, M., Cioni, R., 2007. Breadcrust bombs as indicators of Vulcanian eruption dynamics at Guagua Pichincha volcano, Ecuador. Bull. Volcanol. 69, 281–300.

Wright, H.M.N., Folkes, C.B., Cas, R.A.F., Cashman, K.V., 2011. Heterogeneous pumice populations in the 2.08-Ma Cerro Galán Ignimbrite: implications for magma recharge and ascent preceding a large-volume silicic eruption. Bull. Volcanol. 73, 1513–1533.

Zheng, G., List, R., 1996. Convective heat transfer of rotating spheres and spheroids with non-uniform surface temperatures. Int. J. Heat Mass Transf. 39, 1815–1826.